# Tactile Sensing System Integrated to Compliant Foot of Humanoid Robot for Contact Force Measurement

Ashrarul Haq Sifat

Thesis submitted to the Faculty of
Virginia Polytechnic Institute and State University
in partial fulfillment of the requirements for the degree of

Master of Science
in
Electrical Engineering

A. Lynn Abbott, Chair
Tomonari Furukawa
Ryan K. Williams

December 12, 2018
Blacksburg, Virginia

Keywords: Robotics, Humanoid Robots, Tactile Sensors, Additive Manufacturing of Soft Tactile Sensors, Artificial Neural Networks, Force Measurement

# Tactile Sensing System Integrated to Compliant Foot of Humanoid Robot for Contact Force Measurement

Ashrarul Haq Sifat

(ABSTRACT)

Human beings have a touch and force estimation mechanism beneath their feet. They use this feeling of touch and force to maintain balance, walk, run and perform various agile motions. This paper presents a new sensor platform beneath the humanoid feet, enabled by a pragmatic model based compliant foot design and sensor configuration that mimics the human tactile sensory system for contact force measurement in humanoid robots. Unlike previous force sensor based approaches, the system is defined as a total and sufficient method of Ground Reaction Force (GRF) and Zero Moment Point (ZMP) measurement for balancing and walking using contact force feedback in mid to full sized humanoids. The conventional systems for the GRF and ZMP measurement are made of heavy metallic parts that tend to be bulky and vulnerable to inertial noises upon high acceleration. In addition to low cost and reliable operation, the proposed system can withstand shock and enable agile motion much like humans do with their footpad. The proposed foot is manufactured using state-of-the-art technique with elastomer padding which not only protects the sensors but also acts as a compliance beneath the foot giving integrity in structural design. This composite layer provides compliance and traction for foot collision while the contact surfaces are sampled for pressure distribution which can be mapped into three axis force and ZMP. A single step training process is required to relate the sensor readings to force measurement.

The system's capability of contact force measurement, subsequent ZMP estimation is experimentally verified with the application of appropriate software. Moreover, a simulation study has been conducted via Finite Element Analysis (FEA) of the footpad structure to analyze the proposed footpad structure. The experimental results demonstrate why this can be a major step toward a biomimetic, affordable yet robust contact force and ZMP measurement method for humanoid robots.

This work was supported by the Office of Naval Research, Grant N00014-15-1-2128 as part of development of Project SAFFiR (Shipboard Autonomous Firefighting Robot).

# Tactile Sensing System Integrated to Compliant Foot of Humanoid Robot for Contact Force Measurement

Ashrarul Haq Sifat

(GENERAL AUDIENCE ABSTRACT)

How we interact with the surfaces in contact with us has a crucial role for balancing and walking with agility. The biological touch and force measurement systems in human is currently unmatched, not even mimicked in a significant way in the state-of-the-art humanoid robots' systems. Human beings use this feeling of touch and force beneath the feet to maintain balance, walk, run and perform various agile motions. This research aims to find a holistic system in humanoid robot's feet design that can mimic this human characteristics of force estimation beneath the feet and using that estimation for balancing and walking. A practical model based sensor configuration is derived from the rigorous study of human and humanoid robot's feet contact with the ground. The sensors are tactile in nature, and unlike previous below feet based approaches, the system is defined as a total and sufficient system of Ground Reaction Force (GRF) and Center of Pressure (CoP) measurement. The conventional systems for this purpose are not only highly expensive but also having error in quantification during accelerated movement. The proposed foot is designed following the practical model derived and manufactured using the state-of-the-art mechanism for having a soft cushion between the sensors and the contact surfaces. In addition to low cost and reliable operation, the proposed system can withstand shock and enable agile motion much like humans do with their footpad. The quantification of the forces and pressure from the sensor readings and developed using appropriate software and algorithms.

The system's capability of contact force measurement, subsequent Center of Pressure measurement is experimentally verified with the application of appropriate software. Moreover, a simulation study has been conducted of the footpad structure to analyze the proposed footpad structure. The experimental results demonstrate why this can be a major step toward a biomimetic, affordable yet robust contact force and Center of Pressure measurement method for human-like robots.

# Acknowledgments

I would like to thank my parents and brothers for their limitless support. I could not have succeeded without their constant encouragement throughout the years. Also big gratitude to my wife Aevelina Rahman for her support both academically and mentally.

Thanks to my co-advisor, Dr. Tomonari Furukawa, who provided me the opportunity to work on humanoid robots in the first place. I am very grateful for the guidance, resources, and advice that have been provided to me by his experience.

Thanks as well to Dr. Lynn Abbott and Dr. Ryan Williams for lending their time and wisdom to my research and defense. Thanks to my lab mates in CMS lab who shared a common goal of building exciting, new robots despite the many challenges and setbacks along the way. The informal environment, creative culture and side projects have always made the lab a fun place to work.

Finally, I would like to thank Virginia Tech, the Office of Naval Research, and all the students who came before me for providing this opportunity to work on humanoid robotics in the first place: it has been a dream come true.

# Contents

# List of Figures

# List of Tables

# Chapter 1

# Introduction

## 1.1 Humanoid Robots

The progression of modern robotics has evolved beyond traditional fixed-base robots in the wake of continued research into floating-base systems. Robots which move freely in an unstructured environment, traverse rough terrain, and properly function in complex or hazardous conditions provide promising opportunities to many fields of research and industry. In this aspect, many platforms tend more toward wheels and treads rather than legs. These robots however, perform poorly in complex unstructured environments compared to their legged counterparts [2]. Although most wheeled platforms do not need to address the complexities of software and fall prevention, they also encounter a great deal of difficulty performing agile motions like humans .

A humanoid robot is theoretically capable of addressing all of these scenarios with the same ease and efficiency as the human for whom such structures were designed. Due to this flexibility, bipedal platforms continue to garner the focus of modern robotics. However, the prospect of legged locomotion gives rise to a lot of complexities in design and software implementations and needs substantial improvements to really become as efficient as the inspiration it is built from. Among many other areas to improve, the sensing methodologies in different parts of the humanoid still falls quite far behind the sophisticated system of humans. In this regard, the contact force mea-

surement mechanism utilizing the touch and force feedback beneath the foot remains as one of the most important sensing areas for the humanoid locomotion. This measurement includes the ZMP and multi-axis Ground Reaction Forces (GRF).

As bipedal robots progresses beyond the infantile stages of venturing within laboratory environments, the sensing systems need to continue pushing the limits of the adaptability of their hardware design and software.

## 1.2 Significance of Foot Contact for Humanoid Locomotion

Highly agile walking and balancing imposes great demands on the diverse capabilities of humanoid feet. Human beings utilize the touch and force estimation mechanism under their feet for this purpose. The flexible foot sole of human in conjunction with various kinds of footwear enable us to provide traction in unstructured environment and shock absorption through the medial and longitudinal archs [3] to some extent. It also can adapt to the contours of the ground, sense the surface roughness and adapt to changes [4], [5]. Thus, the feet serve several functions during locomotion of humans that are unmatched by current legged humanoids. The force sensor in the footpad must have high dynamic range in both normal and shear directions to detect emerging slip and for the robot to implement corrective measures to remain upright [6]. However, while maintaining balance, the foot still needs to absorb shock from impact and protect its internal materials. In addition, the foot has to be lightweight to reduce rotational inertia while moving which would lead to reduced burden on the leg actuators. This set of diverse requirements are not easily achieved by the conventional sensing methodologies.

Primarily, the mechanism of contact force and ZMP measurement and application of contact forces are crucial for anthropomorphic force-controlled agility of legged humanoids. The contact force or GRF and ZMP measurement techniques has seen rapid development using MEMS technology [7] and a plethora of systems [8], [9] use the commercially available expensive parts for reliable state estimation for balancing and walking. However, an appropriate modeling of contact points

and optimized foot design which has an integrated force measurement mechanism with it can essentially generate the enhanced hardware necessary for human-like agility at a much lower cost. Introducing elastomer materials in conjunction with biomimetic design can also lead to innovative soft joints that reduce wears or shock and extends the lifetime of hardware. Inspired by this human characteristic, we propose a novel biomimetic low-cost mechanism and hardware of GRF and ZMP measurement for the humanoid robot.

## 1.3 SAFFiR Project Overview

Initiation of this work is primarily motivated by the Office of Naval Research (ONR) Shipboard Autonomous Fire Fighting Robot (SAFFiR) project. The ultimate goal of SAFFiR is to avoid risking human safety while preventing or suppressing danger aboard a naval vessel. To that end, members of the Virginia Tech Dept. of Mechanical Engineering robotics research facilities created humanoid robot platforms capable of performing patrol tasks and addressing potentially hazardous operations. The first approach of this project resulted in the development of the THOR (Tactical Hazardous Operations Robot) platform [10]. Following this, the team had entered into the competition created by Defense Advanced Research Projects Agency (DARPA). The DARPA Robotics Challenge (DRC) was created to drive scholarly and corporate groups toward the cutting edge humanoid robotics research. The challenge was intended to test independent robot's capacity to explore a disaster response area and perform manipulation and locomotion assignments related with such an unstructured domain. Utilizing the information picked up by the advancement of the THOR humanoid, the Virginia Tech DRC group (Team VALOR) made another, progressively competent robotic platform, the Electromechanical Series Compliant Humanoid for Emergency Response (ESCHER) humanoid [11] for use in both the DRC and the SAFFiR project. Among ESCHER's numerous advantages over the previous platform were the ability to operate on battery power and the addition of two adroit mechanical arms provided by HDT Global. Though these platforms are very capable of collection of tasks that comprised the DRC, it was not ideally suited to the SAFFiR project's interests. This provided the opportunity to improve upon many areas including the sensing system and adjustable hardware.

Despite its high performance and novel design, ESCHER faces the problem of inflexibility, complex mechanism, time-consuming operation and trouble-shooting. Our newly designed humanoid ATHENa (Adjustably designed Torque controlled Humanoid for the Environment of NAvy) has the focus of addressing all those issue and at the same time achieve disaster response capability through technology transfer from mid-size to full-size torque controlled humanoids. ATHENa can be used alternately both as a torque controlled and position controlled humanoid. The design criteria of it is to have an easily adjustable structure, high reliability, lightweight and at the same time affordability and high performance through flexible, modular design using 3D printed parts, carbon fiber links and various other innovative design. The mechanism of state estimation falls right into that mission which is described in this thesis. The system of ATHENa provides with the perfect opportunity to demonstrate the compliant foot design with integrated tactile sensing system.

## 1.4 Thesis Objectives

The ultimate goal of the research is to have human-like agility in humanoid robots. Having anthropomorphic fore controlled agility requires the conjunction of many steps. Among those the focus in this research is on the footpad GRF and ZMP measurement mechanism of humanoid as it plays a vital role in the stability during agile motion. The objectives of this thesis are defined as below and the approach and performance evaluation is discussed throughout the remaining chapters.

1. Investigate the modeling of humanoid foot contact points, compare with human anatomy and find out appropriate modeling of humanoid foot contact points in the perspective of GRF.

2. Develop a holistic approach towards below foot integrated tactile sensor based multi-axis GRF and ZMP measurement technique with state-of-the-art manufacturing of complaint soft foot.

3. Evaluate sensor performance as well as adjustable design parameters and structural integrity with appropriate software implementation through simulation and hardware experiments.

## 1.5 Summary of Original Contributions

This paper presents a realistic pressure point based foot design integrated with a tactile sensor system. This is a new approach for humanoid robots to develop a robust, lightweight, resilient GRF and ZMP measurement solution below foot suitable for anthropomorphic force controlled agility. The use of tactile sensors eradicates inertial noise while being able to measure large normal and shear forces to construct the friction cone, detect slip during agile movement and give an accurate estimate of ZMP. The original contribution can be stated as follows:

1. Footpad pressure point based modeling of contact points beneath humanoid foot.
2. Compliant foot design with embedded tactile sensor system for humanoid robots.
3. Technique for tactile sensor based GRF and ZMP measurement for humanoid robots conforming to the conventional theoretical framework for humanoid contact forces.

## 1.6 Approach

The design inspiration is from the biological skin's mechanoreceptors that measure forces by multiplicity of sensing deformation and vibration of the skin layer and also provide traction, compliance, and protection of the mechanoreceptors. The hardware configuration is derived from a comprehensive study of the underlying physics for the GRF and modeling of foot contact pressure points from a pragmatic biomimetic approach. It is also experimentally verified why this model is more suitable than the existing contact models. Off-the-shelf and highly reliable components are used as sensors and a calibration mechanism as well as artificial neural network(ANN) is used to characterize the sensors. Furthermore, the system has adjustable design parameters that make it suitable for any kind of humanoid. The sensor hardware and foot design would be experimentally verified in the newly built ATHENa which has just started walking. The end goal is to enable the human-like agility through multi-axis force and ZMP measurement while being lightweight, capable of absorbing shock and gain traction while walking. Moreover, the structural integrity of the system has also been validated through hardware testing as well as FEA simulations using

COMSOL multiphysics. The performance of the footpad sensing system has been compared with a similar platform of force measurement.

## 1.7 List of Publications

1. Ashrarul H. Sifat, Tomonari Furukawa. A Tactile Sensor Integrated Compliant Foot Design for Humanoid Robots. In Advanced Robotics Journal (in preparation).

2. Jeeseop Kim, Yuki Omori, Ashrarul H. Sifat, Tomonari Furukawa, Adjustably Designed Torque Controlled Humanoid Platform, In International Conference on Control, Automation, Robotics and Vision Engineering, Wasington DC, USA, 2018.

## 1.8 Thesis Outline

The remainder of this thesis is separated into 6 chapters, beginning with a review of the literature and underlying concepts applicable to this thesis, before explaining the original contribution of this work and the resulting experimentation derived subsequently. These contents are organized in as follows:

**Chapter 2** provides a brief literature review exploring prior works in the development of multi-axis contact force measurement with specific focus on those pertaining to biped systems and enabling agile motions.

**Chapter 3** describes the theoretical overview of contact forces, mathematical formulation of the contact forces in the feet and ZMP estimation. It also describes in what way this measurement data would be used in the whole body control framework of the humanoid which ultimately leads to the motions.

**Chapter 4** discusses the hardware design in details with sensor configuration and proposed biomimetic model to justify it. It is built upon a rigorous analysis of humanoid and human foot.

**Chapter 5** includes the experimental study to prove that the proposed method is desirable to humanoids. It includes the sensor characterizations as well as multi axis GRF measurement performances. It concludes with a structural analysis of the proposed foot design.

**Chapter 6** concludes all the results with a glimpse of how this can be made a robust system with flexibility, scalability and also introduces the further studies and applications of this system.

# Chapter 2

# Literature Review

This chapter starts with a brief survey of humanoid robotics, followed by an overview of humanoid foot design with a focus on force measurement strategies. Then some discussion on conventional and alternative contact force sensing mechanisms are discussed. The literature review concludes with a discussion of recent implementations of holistic GRF and ZMP measurement mechanism that integrate sensors with hardware in agile four legged robots.

## 2.1 Humanoid Robotics

The area of humanoid robotics attracts many fields of research. In order to describe the humanoid foot design in the GRF and ZMP context, an adequate literature review on the humanoid platforms is conveyed here at first. Therefore, the content of this section is subdivided into two parts; to discuss humanoid robots in general and a focused survey on the foot design for state estimation purposes.

### 2.1.1 Humanoid Robot Platforms

The methodology towards humanoid robotics was started after research on a few bipedal walking robotic platforms starting in the late 1960's with the Waseda Legged Platform [12]. Researchers

at Waseda University began development of the biped WABOT 1 [13], the first robot designed to mimic human legs. In spite of the fact that this early design of humanoid robotics was crude in its usage, just replaying preplanned development movement without environmental compliance, it impelled the innovation forward, leading to the continued development of the WL and Waseda Biped Humanoid (WABIAN) robot families [12]. During the following decades, humanoid platforms continued to proliferate throughout Japan, leading to the development of such platforms as the Hitachi WH-11 [14], the BLR-G2 [15]. Moreover the early implementations were initiated that would eventually become Honda's ASIMO Humanoid[16]. As research of bipedal humanoids has turned out to be more standard universally, there have been various notable humanoid robots all through the world, some of them even outside of Japan. Boston Dynamics was responsible for bringing in arguably the most popular robot platform of the decade, the Atlas Robot [10], as well as tendril robot platforms such as PETMAN [17]. In spite of the fact that early versions of the ATLAS were noisy and cumbersome, the new DRC Atlas was produced to be smaller and calmer, utilizing electrical power for pressure driven actuators to provide an extremely capable platform to utilize indoors and outdoors. Another robot platform, THORMANG [18], developed by ROBOTIS Platforms, was used by numerous teams in the DRC as a reliable hardware platform. Other notable humanoid research platforms include the German Aerospace Center's Torque Controlled Humanoid, TORO, [19], the Italian Institute of Technology's WALK-MAN [20], Korea Advanced Institute of Science and Technology's HUBO [21], HRP Series [22], and, of course, Virginia Polytechnic Institute and State University's ESCHER [23] platform.

### 2.1.2 Biomimetic Foot Design

Well designed foot plays a crucial role in stabilization control for humanoid robots. There has been sporadic studies on biomimetic foot design both from design perspective and even more so in contact force measurement paradigm. P2 [16] used a type of mechanism formed from rubber bushes inserted into a guide to absorb the landing-impact force. It deforms elastically in the vertical direction upon a force being transmitted from the sole. There are four pieces of rubber bush between the foot sole plate and the six-axis force/torque sensor in each foot of HRP-2 [22], which are effective in reducing the landing-impact force and torque. WABIAN-2R [12] had one additional

passive joint for bending toe motion within its foot. The passive joint was selected as the toe joint based on human gait analysis reports in order to walk with heel-contact and toe-off motions in steady walking. The foot of humanoid robot BIPMAN [24] was made as close as possible to a real foot by making a biomechanical analysis of the human foot. Three types of sensors are associated to this foot including linear resistors, pressure sensors and force/torque (F/T) sensors. Most of these studies focus mainly on the mechanical design and actuation of the human foot without much regard to the sensing aspect beneath it.

## 2.2 Development of F/T Sensors

In many high performance systems, such as the ESCHER [11], HRP2 [8], TORO platform [9] the GRF and ZMP measurement is solely dependent on an expensive but accurate F/T sensor mechanism. However, these rigid and metallic parts are incapable of shock absorption as well as incorporating inertial noise and heavy weight.

The conventional F/T sensors use silicon strain gauges and are commonly used to perform both feedback control and gait analysis in legged robots. However, these commercial sensors have limitations in highly dynamic applications. To quantify GRFs, commercial F/T sensors are frequently utilized in arrangement with a robot's feet, yet at the expense of higher leg inertias and higher impact masses, making the robot less equipped for dynamic movements. Some more examples of robots that incorporate a F/T sensor in each foot for sensing GRFs are 'ASIMO' [16], 'KHR-3 Hubo' [25], 'iCub' [26], 'LOLA' [27], 'BHR-2' [28] and 'WABIAN-2' [29] . The F/T sensor is either obtained commercially, or incorporated into the robot by measuring the deformation of rigid metal structures with semiconductor strain gauges [26]. Furthermore, the mass of the F/T sensor at the distal end of the leg essentially builds the leg inertia, and is inclined to encountering inertial noise amid high impact and fast movements, the two of which happen all the time during agile motion. Specifically, the inertial noise is highly undesirable as it might create false positives for the event of ground contact, which may cause dangers in the framework controller [**?**]. Such events have been experimentally verified in a commercial F/T sensor under shaking [30]. Hence it is not

viable to use F/T sensors for high speed locomotion and an alternative force sensing method is needed [31].

## 2.3 Alternate Force Measurement Solutions

Very few systems have targeted the under-foot plane for placing sensors for GRF and ZMP measurement which could be an alternative to the expensive F/T sensor system. The Darwin-Op platform [32] has introduced piezoelectric force sensors under the feet which can perform qualitative walking state determination but cannot measure GRF and ZMP. In Nao [33], Force Sensitive Resistors (FSR) are used to estimate qualitative walking states and falling down scenario quite smoothly. But both of these systems are only good for qualitative state analysis and do not have enough accuracy for estimating ZMP and contact forces which the multi axis F/T sensors are able to. These below-foot systems are also unsuitable for mid to full size humanoids because of their low range and reliability.

Researchers have attempted alternative strategies for force sensing, for example, utilizing force detecting resistors, contact switches or a mix of various sensors, yet with restricted degrees of progress. Legged robots such as 'H6' and 'H7' [34], [35] use force sensing resistors (FSRs) to do force sensing in the foot, but this could only measure the GRFs in the normal direction [36]. FSRs fail under large shear forces, so they are not suitable for fall detection and enable agile motion. Some legged robots rearrange things further by swearing off with force sensors totally and simply managing with basic contact switches [37], [38]. This makes it difficult to control the robot on surfaces where the friction contrasts from typical (i.e., on a wet or sandy floor with low friction or on slanted or uneven surfaces) [39]. Soft sensing techniques have been explored by Park et. al. in the form of a custom-built strain sensor developed for use in an active soft orthotic device [40]. This in combined with their hyperelastic pressure sensor [41] could form a soft artificial skin with conductive liquid metal channels capable of multi-modal sensing [42]. Correspondingly, the exoskeletal end-effectors implanted with optical fiber Bragg grating sensors permitted Park et al. to incorporate detecting while at the same time limiting the massiveness of equipment[43]. Kuehn

et al. underlines the significance of detecting in the foot, and thus their quadrupedal robot contains numerous sensors in the foot, for example, a F/T sensor, a variety of 49 FSRs, an accelerometer, an absolute angular encoder and a proximity distance sensor [44]. These sensors are utilized to quantify GRFs and identify impacts. All things considered, this extensive number of sensors incorporated in the foot lessens the structural integrity, drives up the expense of the robot, and still experiences the inertial noise issues related with the utilization of F/T sensors as portrayed previously. Therefore, there is still a need to develop a force sensor capable of measuring high loads accurately while undergoing high speed locomotion.

## 2.4 Recent Approaches on Force Sensing

Current research about in tactile sensing has brought about both high force detecting in a single axis as well as in multiple axes. However it is still not suitable or appropriate for the necessities of rapid movement in humanoids. Mei et al. have developed a MEMS tactile sensor that is capable of measuring up to 50N in the vertical direction and 10N in the horizontal directions [45]. However, typical loads are much higher in legged robots. A survey of multiple tactile sensors by Dahiya et al. [46] and Yousef et al. [47] depict that most tactile sensors are not capable of measuring forces above 10N. While this and other comparable arrangements are appropriate for tactile sensing in robotic manipulators, there is still a lot to be wanted while thinking about the dynamic prerequisites of the foot on an agile robot. It is attractive to remove just the fundamental estimations and limit the requests put on the control framework, which must measure the GRFs continuously amid agile motions.

Recently, Chuah *et al.* [48] has introduced a robust footpad design for GRF measurement in highly agile four legged MIT Cheetah using the application of tactile sensing. This system is capable of shock absorption using soft materials as integral part of sensor but optimized for only the four legged animal-like agile robots. There are also recent studies on inexpensive F/T sensors utilizing the MEMS technology and soft materials [49]. But again, these systems are not customized for the application of GRF and ZMP measurement beneath the foot while introducing true human like agility in legged humanoids. It is for the absence of lightweight, robust and fast response

that Tajima *et al.* did not use this kind of force sensing below feet for his running experiments [50]. All in all, it is noteworthy that the extensive use of force sensing below feet as well as biomimetic modeling and configuration of sensors beneath the humanoid foot as a standalone system for anthropomorphic balancing and walking has never been utilized.

# Chapter 3

# Contact Forces of Humanoid

This section describes the tactile sensing methodologies of contact forces as well as the contact dynamics of humanoid robots. Discussion of the contact dynamics and subsequent ZMP analysis gives an insight into how to accurately measure the GRF and ZMP using tactile sensors. Finally an overview of the robot walking states and the importance of contact forces in whole body controller of the robot is also presented in this chapter.

## 3.1 Dynamics of Contact Forces

The Lagrangian dynamics of the whole body motion considers an articulated body consisting of $P$ parts with $N$ degrees of freedom (DoF). Thus, it comprises of $N-6$ joint angles and 6 DoFs for the global position and orientation of the root of the kinematic tree which is usually the pelvis joint or an extremity like hand of foot. The formulation expresses the configuration of the body in terms of its generalized joint angles, $q \in R^N$. These are governed by the $N$ second order differential equations given by,

$$\mathbf{A(q)}\ddot{\mathbf{q}} + \mathbf{b}(\mathbf{q}, \dot{\mathbf{q}}) + \mathbf{g}(\mathbf{q}) + \mathbf{J}_c^T \mathbf{F}_i = \tau \tag{3.1}$$

Here, **A(q)** is the joint -space inertia matrix, $\mathbf{b}(\mathbf{q}, \dot{\mathbf{q}})$ is the vector of centrifugal and Coriolis, $\mathbf{g}(\mathbf{q})$

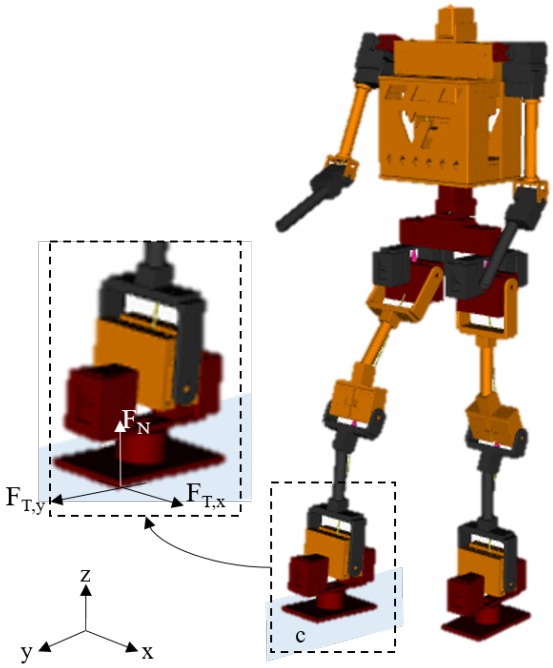


Figure 3.1: Illustration of humanoid robot contact frames. where.

is the gravity vector and $\tau$ is the vector of actuated joint torques. Further, $\mathbf{J}_c$ and $\mathbf{F}_i \in \mathbb{R}^3$ are the point Jacobians and corresponding reaction forces at each contact point, $\mathbf{p}_i \in \mathbb{R}^3$ [51] as depicted in Fig. 3.2 .

A recent study has divided the contacts into different limbs of the humanoid rather than only footpads and distributed the mapping to the inertial frame $J_c$ [52]. Here the contact points are given by foot contact and non-foot contacts. Our focus is on the foot contact points.

$$\mathbf{F}_i^T = \begin{bmatrix} \mathbf{F}_f^T \\ \mathbf{F}_{nf}^T \end{bmatrix} \tag{3.2}$$

The foot contact force can be further divided into normal and tangential components. That is

$$\mathbf{F}_f = \{\mathbf{F}_{fN}, \mathbf{F}_{fT}\} \tag{3.3}$$

where $\mathbf{F}_{fN} >> \mathbf{F}_{fT}$ considering planar contact surface as depicted in Fig. 3.1. Here the task space of the robots is assumed to be coincidental with the world frame the normal force is along the z direction whereas the tangential force is at the x,y direction. Considering the point mass system with mass $m$ and Center of Gravity(CoG) $\mathbf{c}$, the normal component is the most prominent part of the equation 3.1 and plays a vital role in finding the appropriate joint space variables $\mathbf{q}$. Putting the decomposition back to equation 3.1,

$$\mathbf{A}(\mathbf{q})\ddot{\mathbf{q}} + \mathbf{b}(\mathbf{q}, \dot{\mathbf{q}}) + \mathbf{g}(\mathbf{q}) + \begin{bmatrix} \mathbf{J}_f^T & \mathbf{J}_{nf}^T \end{bmatrix} \begin{bmatrix} \mathbf{F}_f^T \\ \mathbf{F}_{nf}^T \end{bmatrix} = \tau \tag{3.4}$$

From this equation, it can be derived that if the non-foot contacts cease to exist or becomes negligible, $\mathbf{J}_{nf}\mathbf{F}_{nf} \approx 0$. But, the foot contact term

$$\mathbf{J}_f\mathbf{F}_f >> 0 \tag{3.5}$$

is very large due to its normal component and has to be measured very accurately in order to estimate or calculate the $\mathbf{q}$ values.

In order to control the GRF and center of pressure (CoP) at each support foot the contact force, $\mathbf{F}_i$ is characterized in literature in various ways depending on the control methods in the different kinds of humanoids [53]. A consequence of the structure of the Lagrangian dynamics is that the

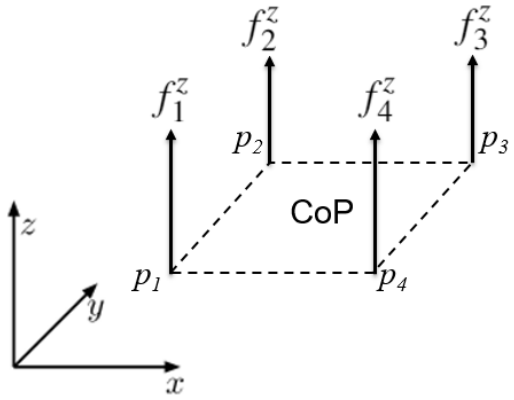


Figure 3.2: Modeling of contact forces to distinct points of the footplate. The CoP is bound to lie in the convex hull of contact points, $\mathbf{p}_i$.

part of this dynamics which is not directly actuated involves the Newton and Euler equations of motion of the robot taken as a whole. The Newton equation can be written in the following way:

$$m(\ddot{\mathbf{c}} + \mathbf{g}) = \sum_i \mathbf{F}_i \tag{3.6}$$

The Euler equation can be expressed with respect to the CoM in the following way:

$$\dot{\mathbf{L}} = \sum_i (\mathbf{p}_i - \mathbf{c}) \times \mathbf{F}_i \tag{3.7}$$

with $\mathbf{p}_i$ the points of applications of the forces $F_i$. Considering a reference frame oriented along the ground, with the z axis orthogonal to it . Without loss of generality, supposing that the points of contact, $p_i$, with the ground are all such that $\mathbf{p}_i^z = 0$. In contact with a flat ground, combining the equations 3.6 and 3.7,

$$m\mathbf{c} \times (\ddot{\mathbf{c}} + \mathbf{g}) + \dot{\mathbf{L}} = \sum_i \mathbf{p}_i \times \mathbf{F}_i \tag{3.8}$$

Equation 3.8 makes it obvious that the robot needs external forces, $\mathbf{F}_i$, in order to move its CoM in a direction other than that of gravity. The control of non-level and non stationary ground at each foot contact and slip estimation can also be followed by the appropriate modeling and application of contact forces. In Fig. 3.1 the contact forces acting on point $c$ are divided into normal and tangential components.

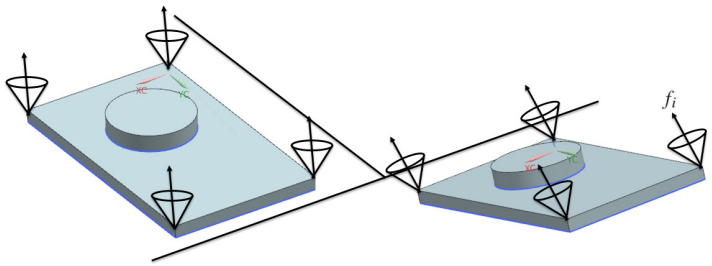


Figure 3.3: friction cone approximation of foot contacts

As mentioned in [54], the structure of the Lagrangian dynamics makes it clear that contact forces are central to the modeling and control of legged robots. Therefore, we need to define the contact force dynamics for stable walking motion. The Coulombs friction force for contact point, $p_i$ gives us the motion dynamics of the contact point, where, for sliding motion if $\dot{\mathbf{p}}_i^{x,y} \neq 0$, then

$$\mathbf{F}_i^{x,y} = -\mu_0 \mathbf{F}_i^z \frac{\dot{\mathbf{p}}_i^{x,y}}{||\dot{\mathbf{p}}_i^{x,y}||} \tag{3.9}$$

In this equation it is assumed that foot is planted on the planar ground, such that $p_i^z = 0$. $\mu_0 > 0$ the friction coefficient with respect to the robot feet to the isotropic ground surface. Furthermore, for non-sliding motion, if $\dot{\mathbf{p}}_i^{x,y} = 0$, then

$$\mathbf{F}_i^{x,y} \leq \mu_0 \mathbf{F}_i^z \tag{3.10}$$

To constrain the motion to non-sliding, this is typically referred to as the friction cone as depicted in Fig. 3.3 which determines the bound of the contact force components. It is noteworthy that this friction model directly implies the unilaterality condition which means the contact forces are usually unilateral. The robot can usually push on the ground and not pull from it.

$$\mathbf{F}_i^z \geq 0 \tag{3.11}$$

However, to model the compliant contacts, taking into account the visco-elastic properties of the materials in contact in the direction orthogonal to the contact surfaces, the model is given by (3.12) if $p_i^z \leq = 0$.

$$\mathbf{F}_i^z = -K_i \mathbf{P}_i^z - \Lambda_i \dot{\mathbf{p}}_i^z \tag{3.12}$$

Here, $K_i$ and $\Lambda_i$ are stiffness and damping coefficients, respectively. This model doesn't satisfy the unilaterality condition (3.11). Therefore, the normal force, $f_i^z$ , can be the result of a penetration of the contact point below the contact surface, i.e. when $\mathbf{p}_i^z \leq 0$.

In the case of rigid contact modeling Equation (3.10) is applicable to rigid contact modeling where no penetration of the contact points below the contact surfaces are considered and the unilaterality condition (3.11) is satisfied. To put it more simply, the rigid model can be summarized in the following way:

$$\mathbf{F}_i^z \geq 0, \quad \mathbf{p}_i^z \geq 0, \quad \mathbf{F}_i^z \mathbf{p}_i^z = 0 \tag{3.13}$$

Here, both the normal force, $\mathbf{F}_i^z$ , and the position of the contact point with respect to the contact surface, $\mathbf{p}_i^z$ , must be non-negative, but at least one of them must be equal to zero which is known as the complementarity condition.

The modeling of contact force in the context of biped walking is discussed in [22], [53].

$$\mathbf{F}_i = \sum_{j=1}^{4} \beta_{i,j} \rho_{i,j} := \beta_i \rho_i \tag{3.14}$$

Here, each GRF is modeled using four basis vectors $\beta_{i,j}$ and their magnitudes $\rho_{i,j}$ that approximate friction cone on the ground

$$\beta_{\mathbf{i,j}} = [\beta_{i,1}, .., \beta_{i,4}] \tag{3.15}$$

The columns of $\beta_{i,j} \in \mathbb{R}^{3\times 4}$ are unilateral bases that span the volume of admissible forces in inertial coordinates. $\rho_i \in \mathbb{R}^4$ is the generalized contact forces, a vector of non-negative coefficients to be determined via the whole-body controller.

## 3.2 ZMP Estimation

The Zero-Moment Point, or ZMP, is the point on the surface of the foot where a resultant force R can replace the force distribution shown in Fig. 3.4 [1].

In Fig. 3.4 an example of force distribution across the foot is given. As the load has the same sign all over the surface, it can be reduced to the resultant force R, the point of attack of which will be in the boundaries of the foot. Let the point on the surface of the foot, where the resultant R passed,

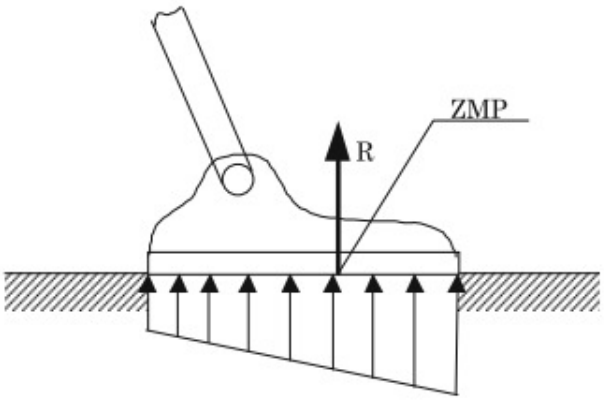


Figure 3.4: Definition of Zero-Moment Point (ZMP) [1]

be denoted as the zero-moment point, or ZMP in short.

As mentioned in [55], by dividing the equation 3.8 by the Newton equation 3.6, the equation of the CoM dynamics in relation to the CoP is given by,

$$\mathbf{c}^{x,y} - \frac{\mathbf{c}^z}{\ddot{\mathbf{c}}^z + g^z}(\ddot{\mathbf{c}}^{x,y} + \mathbf{g}^{x,y}) + \frac{1}{m(\ddot{\mathbf{c}}^z + g^z)}\mathbf{S}\dot{\mathbf{L}}^{x,y} = \frac{\sum_i \mathbf{F}_i^z \mathbf{p}_i^{x,y}}{\sum_i \mathbf{F}_i^z} \tag{3.16}$$

where $\mathbf{S} = \begin{bmatrix} 0 & -1 \\ 1 & 0 \end{bmatrix}$, $\mathbf{c}$ and $m$ are COM position and the point mass of the robot respectively. On the right hand side appears the definition of the CoP, $\mathbf{z}$, of the contact forces, $\mathbf{F}_i$. These contact forces are usually unilateral following (3.11). implies that the CoP is bound to lie in the convex hull of the contact points as depicted in Fig. 3.2. The support polygon which is another important concept is related to the ZMP. As shown in Fig. 3.5, let us consider the region formed by enclosing all the contact points between the robot and the ground by using an elastic cord braid. We call this region as the support polygon. Mathematically the support polygon is defined as a convex hull, which is the smallest convex set including all contact points.

$$\mathbf{z}^{x,y} = \frac{\sum_i \mathbf{F}_i^z \mathbf{p}_i^{x,y}}{\sum_i \mathbf{F}_i^z} \in \ conv\{\mathbf{p}_i^{x,y}\} \tag{3.17}$$

This will be our fundamental equation for calculating the CoP. In stable single support, the foot COP is coincidental with the ZMP [56]. As described in [55], the foot torque can also be calculated from the individual reaction forces and position of the foot.

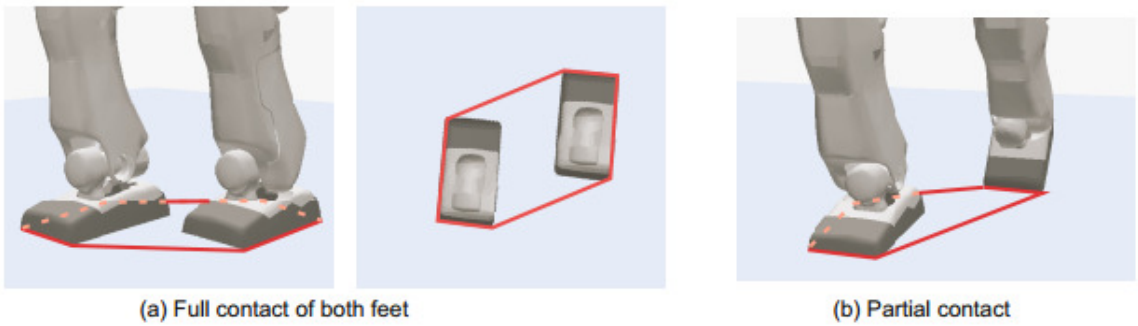


Figure 3.5: Support polygon [1]

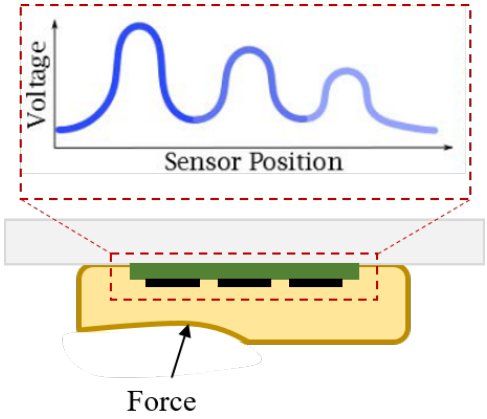


Figure 3.6: Deformation of elastomeric padding. As ground reaction forces are applied to the footpad in this cross-sectional view, the soft elastomer deforms, sending a unique signal, based on the normal and shear components, to the barometric pressure sensor array PCB embedded within.

## 3.3 Tactile Sensing of Contact Forces

There are several technologies for tactile sensing. The transducers produces signals based on these mechanisms. For a rubber casted MEMS barometric tactile sensor, it measures normal stress in the direction normal to the chip package, with insignificant response to normal stresses in the lateral direction or to shear stresses. With the application of the contact force $\mathbf{F} = \{F_x, F_y, F_z\}$, the tactile sensors produce a voltage output as shown in Fig. 3.6. If there is $N$ number of sensors with coupled geometric configuration, then they produce $N$ voltage signals, $\mathbf{V} = \{V_1, ...V_i, ...V_N\}$. These voltage signals are passed through suitable filtering and read through the communication channels as outputs. The voltage signals can be expressed as a function of stresses exerted due to

the external forces, $\sigma$ and the sensitivity $\mathbf{S}$ of the system.

$$\mathbf{V} = f(\sigma, \mathbf{S}) \tag{3.18}$$

Given the spatial configuration of the modules and their transducers, a mechanical analysis can relate the forces applied to the mounting plates to local loads on the transducers, in terms of the geometric design parameters. To relate the local normal stress to the applied load, the normal and shear loading cases must be examined. In densely configured sensors arrays, pure normal load $F_z$ results in equal uniaxial compression of the modules [49]. However, for sparsely populated configurations, the stress is also a function of distances.

$$\sigma_{z,i} = \frac{F_z}{LW} f(p_i^{x,y}) \tag{3.19}$$

where length and width of the contact areas, $L$, $W$ and, the position of the tactile sensor is $p_i^{x,y}$ and

$$S_{F_z,i} = \frac{KF_z}{LWh^n} \tag{3.20}$$

$K$ is a calibration constant that takes into account the effects of the material properties of the rubber being used. For the shear component of the stress however, the length and width of the contact areas do not remain directly inverse proportional.

$$S_{F_{x,y},i} = \frac{KF_{x,y}p_i^{x,y}}{h^n} f(LW) \tag{3.21}$$

Thus assuming super imposable stresses, the voltage output can be related to the applied forces as,

$$\mathbf{V} = \mathbf{UF} \tag{3.22}$$

Where the matrix $\mathbf{U}$ is the collected constrains from the equations 3.20 and 3.21 and has a rank of 3. The constants $W$, $L$, $h$, $K$, $p_i^{x,y}$ are independently tunable to construct the desired characteristics of the system. These equations directly relate each of the design parameters to the sensor output, and can be used to optimize the configuration for a desired sensitivity and range. The final six-axis response can then be calibrated using a standard least-squares fit or other regression techniques to experimental data. An affine term is added to compensate for a fixed offset in the sensor readings. Assuming planar surface, the normal contact force measurement becomes, as depicted in Fig. 3.7,

$$\mathbf{F} = \sum_i F_i \tag{3.23}$$

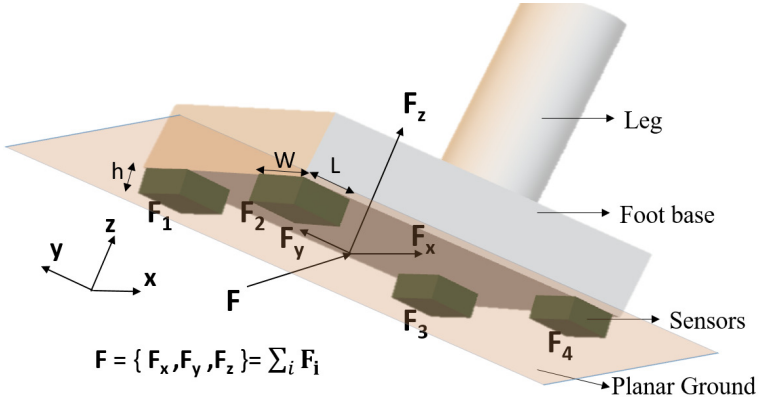


Figure 3.7: Illustration of humanoid robot contact forces on below foot sensors.

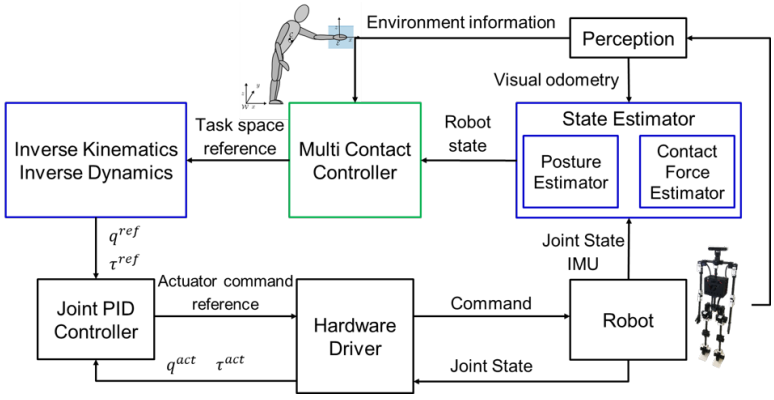


Figure 3.8: Fundamental components in control flow in humanoid robots.

## 3.4 Application in Force Control

GRF and ZMP measurement is one of the fundamental control aspects in the flow of humanoid force control as well. The other parts are Forward / Inverse Kinematics (IK) , Forward / Inverse Dynamics(ID), Optimization, Collision Detector. All of these components has to work together to be able to generate a force controlled motion of the humanoid. With a robust measurement of contact forces, the control scheme can also be extended to the multi contact controller of the humanoid as depicted in Fig. 3.8.

The time varying DCM [57] is derived from the COM position as below

$$\zeta = \mathbf{c} + \frac{1}{\omega}\dot{\mathbf{c}} \tag{3.24}$$

Here $\zeta$ is the capture point which can be defined as a point the COM is converging to.

DCM is moved by controlling the Virtual Repellent Point (VRP)

$$r_{vrp} = \mathbf{c} - \frac{\dot{\mathbf{L}}}{m(\omega^2 - \omega)} \tag{3.25}$$

Using VRP, the first order dynamics of the DCM become

$$\dot{\zeta} = (\omega - \frac{\dot{\omega}}{\omega})(\zeta - r_{vrp}) \tag{3.26}$$

In terms of joint space , Basic equation of CoM dynamics is

$$\Lambda\dot{\mathbf{q}} = \mathbf{h}_G \tag{3.27}$$

$\Lambda$ the centroidal momentum matrix, $h_G$ is the centroidal momentum vector. By differentiating it, we get the relationship between contact forces and joint states.

$$\dot{\Lambda}\dot{\mathbf{q}} + \Lambda\ddot{\mathbf{q}} = \sum_i \mathbf{W}_i\mathbf{F}_i + \mathbf{w}_g \tag{3.28}$$

$W_c$ maps contact forces to wrenches acting about the CoM, and $w_g$ encodes the force of gravity. To prevent slips, the friction cone constraint has to be implemented before the optimization. To minimize the tracking error of each operational goal while satisfying the dynamic constraints, utilize a QP solver to optimize joint accelerations and contact forces

$$\min_{\ddot{\mathbf{q}},\rho} \frac{1}{2}||(\ddot{\mathbf{c}} - \dot{\Lambda}\dot{\mathbf{q}} - \Lambda\ddot{\mathbf{q}}) + \lambda_{\ddot{\mathbf{q}}}||\ddot{\mathbf{q}}||^2 + \lambda_\rho||\ddot{\rho}||^2|| \tag{3.29}$$

Here the constraints for the optimization process is

1. COM dynamics , equation 3.28
2. Joint Limits, $\underline{\mathbf{q}} \leq \mathbf{q} + T\dot{\mathbf{q}} + \frac{1}{2}T^2\ddot{\mathbf{q}} \leq \overline{\mathbf{q}}$
3. Joint torque limits $\underline{\tau} \leq \tau \leq \overline{\tau}$
4. Contact force constraints $0 \leq \rho$

## 3.5 Robot State machine

The walking motion of the robot can be defined in terms of the steps described in Fig. 3.9. The transition between various steps can be described by a finite-state machine that runs on the divergent component of motion (DCM) trajectory planner. To supplement this planner, a fast and accurate feedback of contact forces is needed for the estimation of walking states to the higher level in the control framework.

The basic support phases are the single support and the double support phases. In the double support phase, it is assumed that both the feet are in contact to the ground and the motion is defined to reach particular ground reaction forces for stable support. The contact points in the feet provide these forces. During the beginning of the double support phase, the trajectory planner estimates the next position of the swing foot position and generates a swing foot trajectory. One of the foot then goes to the single support phase through shifting the heel and then toe off. Subsequently, it goes to heel strike and then to double support again, planning for the trajectory of the other foot. In this way, the walking states continue in a cyclic manner. The cycle can be adjusted according to the motion or task which can include multicontact balancing [52], [58], [59] as well as manipulation and walking at the same time. Also as mentioned in [23], the timing and application of contact force is crucial for proper balancing of the humanoid. The transition form heel-strike to swing foot and from heel-strike to double support is greatly influenced by the sufficient loading of the contact forces. Furthermore, abrupt changes to contact force can introduce jerky motions and instability. Therefore for achieving autonomy in walking and balancing, a reliable and accurate estimate of contact forces and walking states are indispensable.

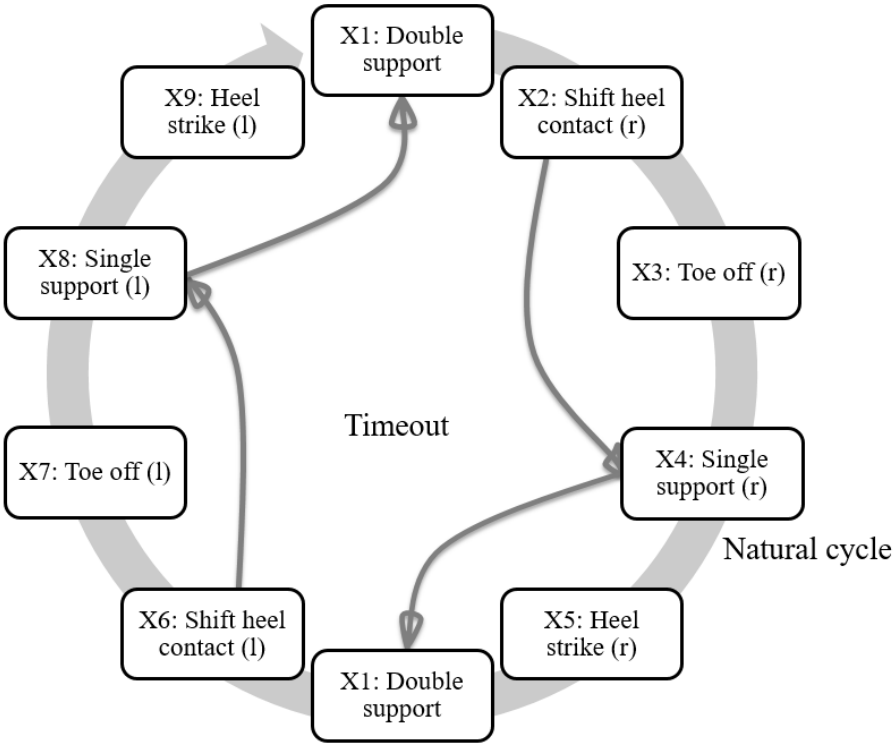


Figure 3.9: Robot states in biped walking motion. The outer directions depicts the natural walking cycle. The inner directions are taken into account when timeout occurs during any of the motions. *l* and *r* stands for left and right foot respectively.

# Chapter 4

# Design and Manufacturing of Compliant Foot

Based on the proposed model of pressure points, a novel compliant foot design has been proposed and prototyped to facilitate force controlled agility through robust state estimation. It also incorporates state-of-the-art manufacturing technique and appropriate software system to characterize the sensors. This chapter describes the hardware design and novelty of our approach.

## Biomimetic Modeling of Humanoid Foot

Human foot has diverse capabilities and subsequently a diverse range of pressure mapping beneath it in reaction to different actions. A wide range of analysis in the medical world has been done to understand the pressure distribution for the treatment of various physiological problems and diseases like arthritis [60],[61]. It is generally analyzed that human foot has two archs, one in longitudinal direction and another in transverse direction [62]. The transverse arch may not be present in many people but the longitudinal arch is prevalent in most of the human foot. Therefore, pressure point distribution is towards the edge of the archs and inhomogeneous throughout the foot pad plane. The simplified pressure distribution is depicted in Fig. 4.1, whereas humanoid robots foot are visible in the friction cone model in Fig. 3.3. The planar humanoid foot however has

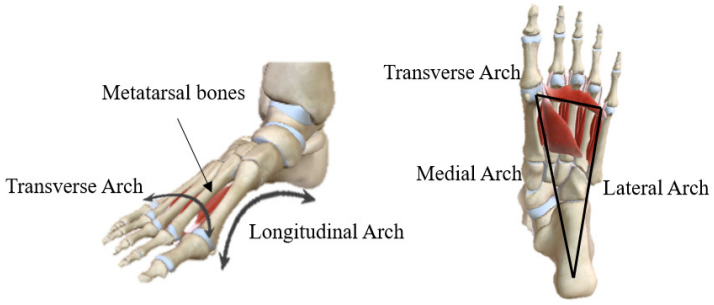


Figure 4.1: Arch in human foot

the pressure distributed throughout the footpad equally unless some unevenness appears due to the terrain. The contact model in widely accepted literature confines it to the four points as shown in Fig. 3.2.

The objective of analyzing the human foot is to investigate the inherent agility of humans in terms of sensor design. For a sensor system to have maximum applicability, it needs to have a realistic model in comparison with similar efficient systems. In this case, the human body is the living embodiment of agility. After careful comparison, it is evident that it is not feasible to have the boundary point based contact point modeling in the humanoids. Therefore, a model is presented of five pressure points beneath the typical humanoid foot which is depicted in Fig. 4.2 deriving from the pressure points of the humanoid foot. The basic difference is that because of the longitudinal and transverse archs, the human foot has a triangular foot plane with no pressure point in the middle of it. In fact, the human foot has the least pressure in the mid point of the footplate. Whereas, in humanoid robots, the middle point is the most sensitive pressure point and the conventional four boundary pressure point based model is not sufficient for a highly effective sensor system for sate estimation. The force distribution under the foot is experimentally determined which verifies the current modeling of pressure points for humanoids. Moreover, placing a fifth sensor right under the base of the leg is crucial for both accuracy and mechanical stability of the foot plate. This configuration is also beneficial to calculate the ZMP using (3.17) without the loss of generality in the method of calculation.

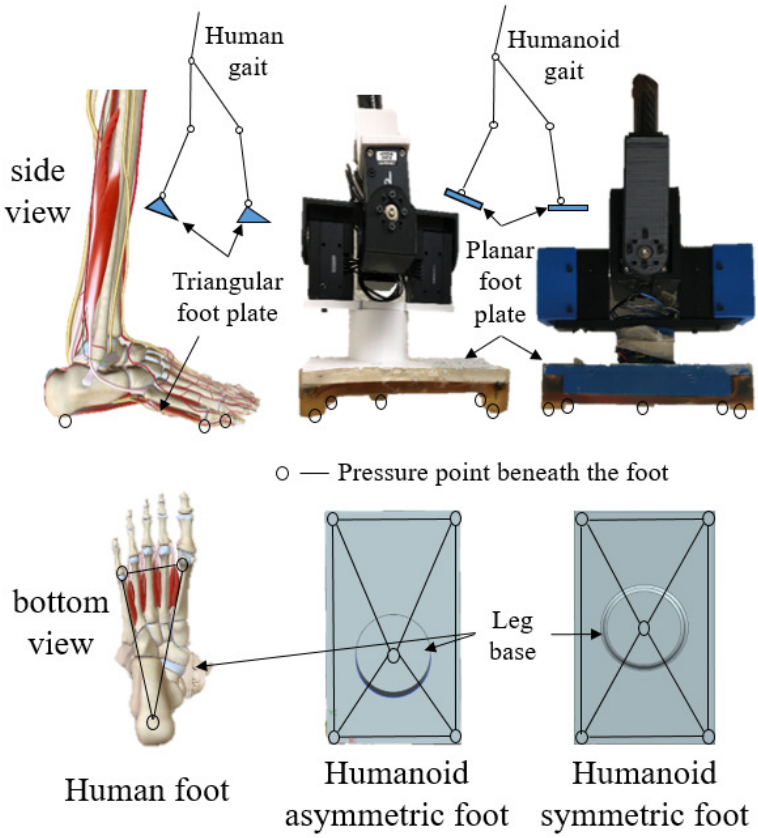


Figure 4.2: Pressure points under human foot(left) vs pressure points under humanoid foot (middle and right)

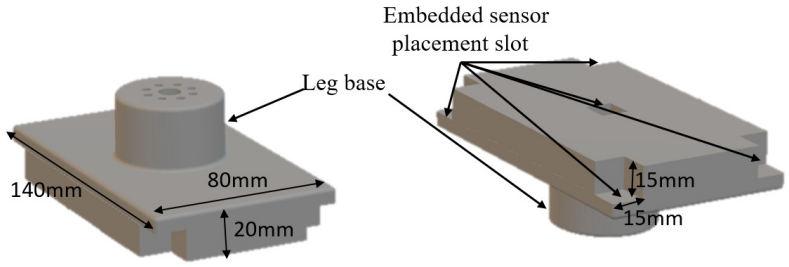


Figure 4.3: CAD design of foot skeleton before casting with elastomer, isometric view(left) and vertically flipped isometric view(right).

## 4.1 Skeletal Design of Foot

As visible in Fig. 4.2, the humanoid foot skeleton is designed to accommodate the embedded tactile sensors inside it and an elastomer deposition is enabled up to desired height to match the required specification. Fig. 4.3 depicts the foot design which is carefully constructed to enable suitable weight as well. The sensor placement slots are designed not only to keep the sensors secured, but also to limit height of elastomer padding to the insignificant portion of the sensing areas. The elastomer has a consistency throughout the footpad surface for rigidity and shock absorption. Combining the studies with optimized foot sole design for humanoids [63] would enable this sensor system to serve the purpose of both the state estimation and optimized shock absorption below foot. In the current system, a rubber padding of 5mm is kept throughout the foot sole and 24mm beneath the sensors, 15mm of which is enclosed in two sides by the walls of the extruding feet at the foot corners as can be seen in Fig. 7(b), (c) and Fig. 4.3. The skeletal structure is 3d printed using ABS plastic and proven to be rigid enough to withstand the stress of the system. The capability and effectiveness of this system is presented in the experimental analysis part both in terms of practical walking and simulation.

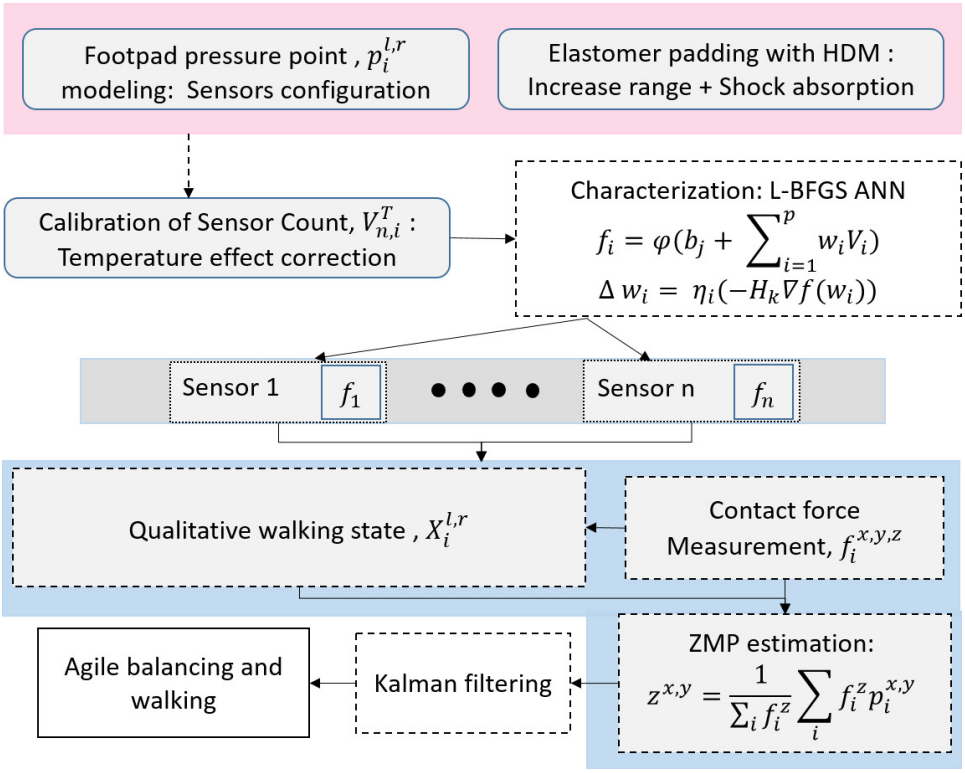


Figure 4.4: Proposed framework for improved force measurement in humanoid robots.

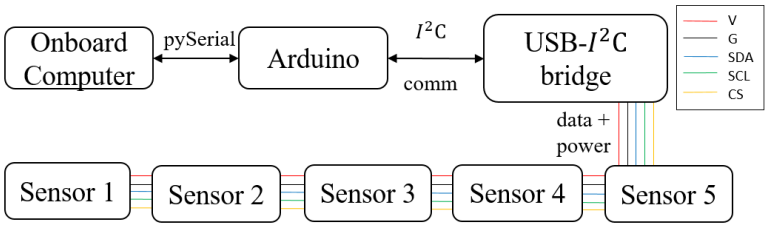


Figure 4.5: Hardware connection diagram.

## 4.2 Mechatronic System Design

The proposed framework is depicted in Fig. 4.4. introducing a holistic approach of tactile sensor embedded compliant foot design for humanoids. The pressure point model described in previous section is the first step of the framework. Next is the appropriate design of hardware and software. Five tactile force sensors in the positions specified by the pressure point model in Fig. 4.2. have been introduced. Among the various force sensors available commercially, the tactile force sensors Takktile, developed by Righthand Labs [64] are chosen for a number of reasons. The main reason is the adjustable range of the sensor and its inexpensive yet well defined usage. It uses high speed $I^2C$ protocol for chip to chip data transfer. In the present study, an Arduino Micro is used as a serial communication device with the on board computer in ATHENa. The underlying technology is MEMS barometric pressure sensors which has a wide range of operation and high durability. The overall electrical system is depicted in Fig. 4.5 which is quite convenient to implement, prototype and troubleshoot.

## 4.3 Elastomer Deposition Technique

The off-the-shelf Takktile sensor has a range of around 1.5N for the commercially available elastomer casting of 3.5 mm. This range is clearly not enough for the current system which weighs around 10 kg. It is known from literature that increasing the rubber thickness increases the range of strain distribution at a cost of slight decrease in sensitivity [64]. It is experimentally verified that a casting 16 mm of elastomer would give a range of 15-16 N and 24 mm would give around 33-35 N for each sensor. This would be sufficient for the current application of operating the lower body

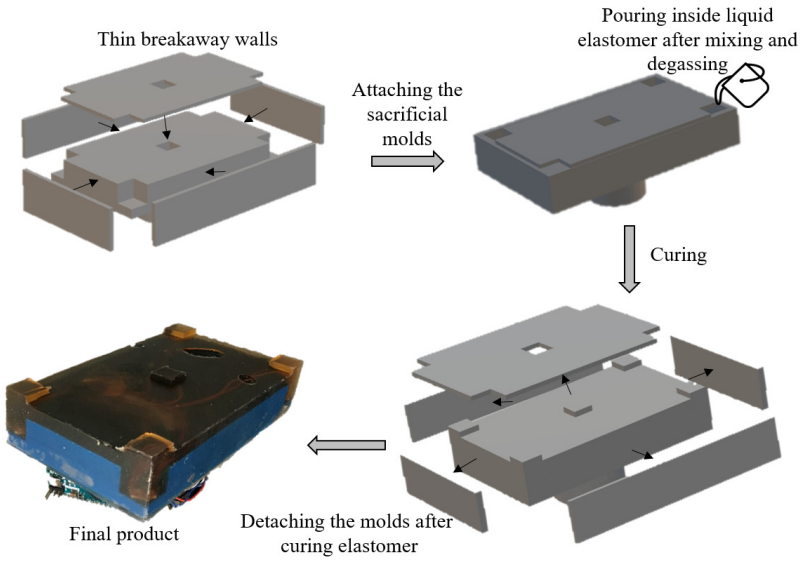


Figure 4.6: HDM technique applied to manufacture soft foot.

of ATHENa. The final version of 24mm elastomer casted sensors will be actually applicable for the whole humanoid as it will have a range of 165-170 N in total for the foot. The same material as the original Takktile strips is used which is Vytaflex 20. It is a two-part room temperature cured polyurethane elastomer. It is also quite inexpensive, has low viscosity for mixing and pouring and mechanically robust after curing. It has a modulus of elasticity is reported to be 280 kPa [64] which gives it shock absorbing capability without much deform for this type of lightweights humanoids. Vacuum degassing is used to get rid of the bubbles forming into layers.

The contact area of the sensor also increases due to the casting of rubber. The contact surface of each sensor in commercially available structure is 5 sqcm. After casting the rubber it has increased to approximately 225 sqcm but the optimum area for the most sensitivity and stability is still an open research area and need formal study to determine.

The molding techniques follows a basic hybrid deposition manufacturing technique [65]. The foot is fitted into the part by part 3D printed mold as shown in Fig. 4.6 . The outer enclosure of walls made also by ABS plastic via 3D printing are called the sacrificial walls. After curing, these are removed from the cast along with another structure that determines the height of the consistent rubber padding throughout the walls and the protrusion of the elastomer right below the

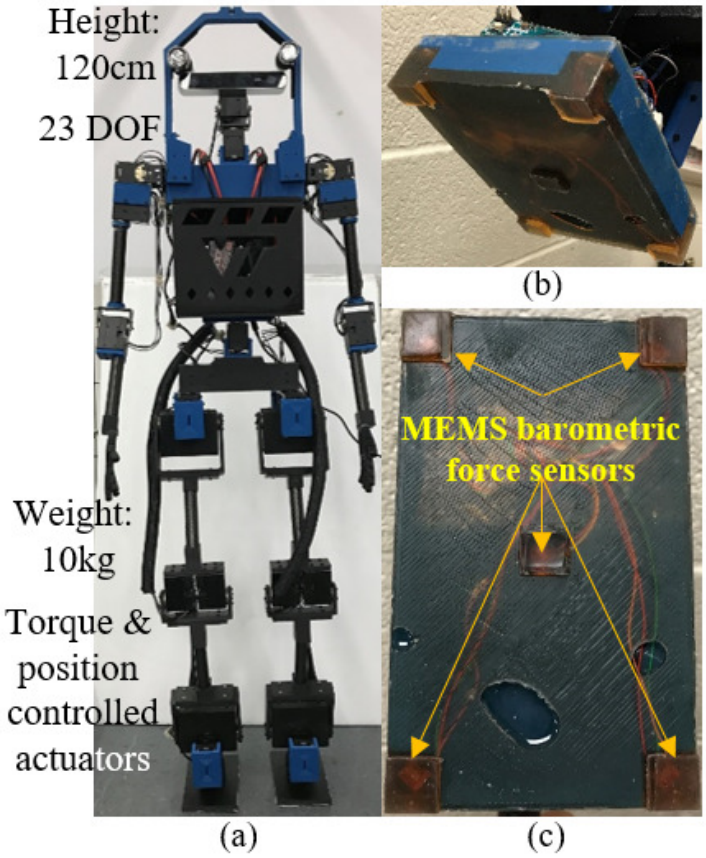


Figure 4.7: (a) ATHENa Humanoid, (b), (c) Tactile sensor platform for state estimation

sensors contact areas. This design is completely adjustable if the range of the sensors need to be increased by just peeling off the rubber from beneath the foot and casting a new one with adjusted mold design. Using a thin plastic coating, the wiring of the sensors are kept separated from the elastomer for easy separation if needed. Moreover, as can be seen from figure, the ground contact surface is isolated between the vicinity of the sensors and the surface is designed like a soccer cleats shoe structure for the sensors to have high effectiveness. The protrusions are not very high so that the stability during walking is not disturbed. Later it is verified in simulation and with predefined experimental walking steps that this combination of elastomer padding is considerably stable as well as maintains a high sensitivity to contact forces.

# Chapter 5

# Experimental Performance Evaluation

This chapter describes in detailed explanation the experimental evaluation procedures and results. It is started with the sensor characterization and evaluating different characterization schemes and their performances. Next is using these characterized models into methods for normal and tangential force measurements as well as ZMP measurement and analysis. The chapter concludes with a preliminary analysis on the structural deformation of the footpad which has a great impact in the whole humanoid systems stability.

The sensors showed significantly satisfactory behavior as predicted with the model based configuration. The noise level of the sensors is also negligible as the sensor arrays already implement a low pass filter in hardware to eliminate noise [64]. The sensitivity and force sensing was tested using three different height specifications. Overall, the parameters of experimentations for verifying the effectiveness of the system is described in table 5.1. The experimental setup is given in Fig. 5.1.

## 5.1 Sensor Characterization

The sensor characterization was done with linear regression for preliminary analysis. Each sensor data was characterized into linear fit function to calculate the model for conversion to force values.

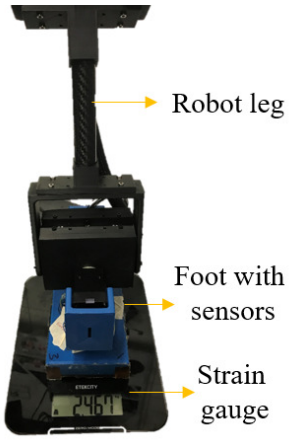


Figure 5.1: Experimental setup for sensor characterization

Table 5.1: Parameters of experimentation

| Parameters | Values |
|---|---|
| Rubber cast Height | 13 to 24 mm |
| Foot design | asymmetric (human-like) vs symmetric |
| Number of sensors | 4 to 5 |
| Estimated Forces | x, y, z axis |

An average value of the two approach of forward and backward propagation of increasing weight to deduce the linear fit model was considered. This was due to the fact that although the hysteresis is very negligible but it is still present at a very low level which is visible in Fig 5.5. The calculated count vs force slopes for the five sensors in the foot with 13 mm height are 39.1, 37.95, 32.38, 51.26, 37.01. These slopes are the linear fit modeling parameters for the sensor count to convert to force values.

In Fig. 5.2, the linear fit graph for both the configurations of 13 mm and 16 mm of rubber cast height are shown. It is visible that the value is saturated for lower force values in the 13mm sensors which is expected.

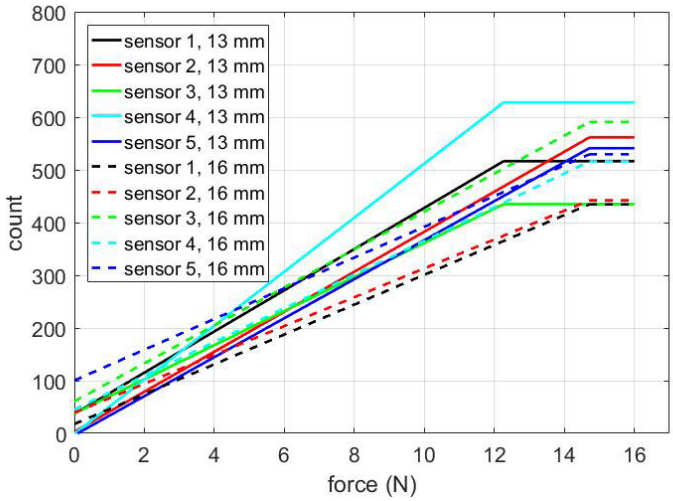


Figure 5.2: Linear fit of sensor values for preliminary analysis.

The sensors have almost linear characteristics in terms of force and voltage counts but there is slight nonlinearity observable as seen in Fig. 5.4 and 5.5 . Moreover, after verifying the contact force estimation with the linear fit model, the estimation accuracy was 98% which can be improved if the nonlinearity are considered. There are several techniques of non linear modeling including system identification through transfer functions which is studied by Chuah et al, [48]. But from a rigorous analysis of similar systems, it is concluded that system identification does not work well for this kind of unstructured prediction. Therefore, taking inspiration of neural network models implemented by Ananthanarayanan et al. [66], the current system is characterized using ANN regression. Subsequently, to collect data for nonlinear modeling, seven to ten test cases of approximately 100 data samples were obtained from the experimental setup of Fig. 5.1 for each sensor. Only one sensor test data is shown in Fig. 5.4 for clarity. The ground truth of force values depicted in red in Fig. 5.4 is taken from a digital strain gauge with 0.0098N resolution by manually putting irregular weights and subsequently recording the voltage count form the single sensor. Likewise, five sensor for each foot is put in the testbed separately and their data taken similarly. The algorithm of experimentation for this ANN is depicted in Fig. 5.3

The five analog voltages are assembled into an array where $v_n$ represents the n-th voltage sample

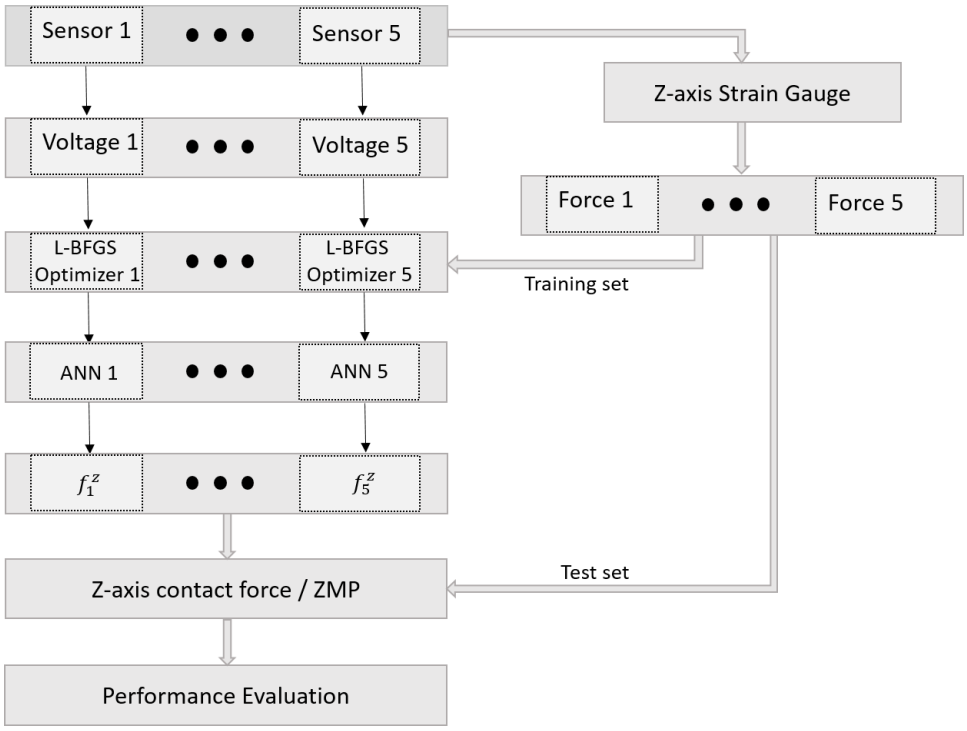


Figure 5.3: Algorithm of fitting sensor data into neural network for force and ZMP estimation.

from the $i-th$ pressure sensor. Here $i \in (1...5)$ and $n \in (1,...,N)$.

$$V_i = \begin{bmatrix} v_1 & \cdots & v_n & \cdots & v_N \end{bmatrix}^T \tag{5.1}$$

The corresponding force vectors are given by a similar matrix for each voltage count, $V_i$ by $F_i$. Here the L-BFGS method is used as the algorithm to train the neural network [67]. The method is very fast and suitable for small datasets with slight non-linearities. For our case, using a dual layer of neurons with 100 nodes in the hidden layer were enough to get considerable accuracy. The ANN uses the following approximation with RELu as the activation function and takes only seconds to complete the training procedure.

$$F_i = \phi(b_j + \sum_{i=1}^{p} w_i V_i) \tag{5.2}$$

Here, the bias term $b_j$ is chosen arbitrarily for the best result and the weight of the hidden layer units, $w_i$ is updated using the approximation of the inverse Hessian of the weight function, $f(w_i)$.

$$\Delta w_i = \eta_i(-H_k \nabla f(w_i)) \tag{5.3}$$

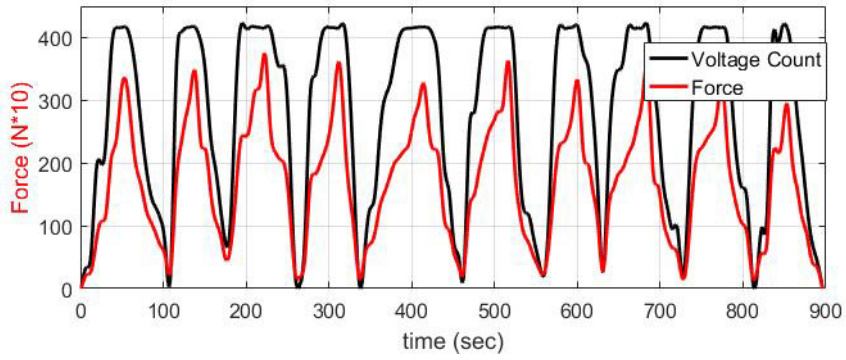


Figure 5.4: Test data from one sensor.

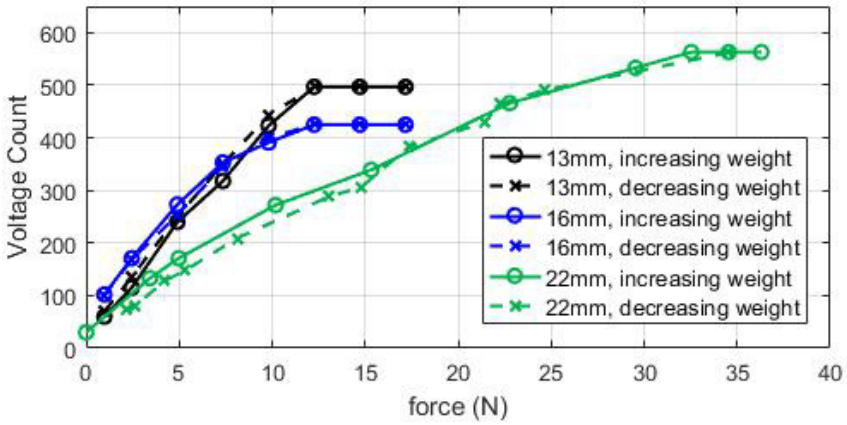


Figure 5.5: Hysteresis curves of the sensors with elastomer casting height of 13mm, 16mm and 22mm.

In Fig. 5.5, the hysteresis curves for the configurations of 13 mm, 16 mm and 24mm of elastomer cast height are shown. It is visible that the value is saturated for lower force values in the 13mm sensors which is expected. It verifies that the rubber height is the adjustable parameter for increasing the range of the sensors. It can be easily achieved by modifying the mold design before 3D printing. Before each run of testing, a calibration is designed that matches zero voltage count with 0 N force as each testing procedure may happen at separate times leading to different zero force readings from the sensor due to temperature effect. This is referred as the temperature effect correction in Fig. 4.4.

## 5.2 Normal Force Measurement

The GRF is measured using the simple kinematic equation in each feet,

$$f_c = \sum_{i=0}^{5} f_i^z \tag{5.4}$$

Each of the $f_i^z$, is measured from each of the sensors using their ANN fit model and $f_c = \{f_l, f_r\}$ is the total contact force of either of the left or right foot. The result of contact force estimate is shown in Fig. 5.6 where about 100 discrete loading and unloading values were used and averaged for both of the 13mm and 24 mm padding of elastomer material. The method of evaluation was calculating the root mean squared error (RMSE), normalized RMSE and the coefficient of determination, $R^2$ which are given by the following equations.

$$RMSE = [\frac{1}{N}\sum_{i=1}^{N}(\hat{y}_i - y_i)^2]^{\frac{1}{2}} \tag{5.5}$$

$$Normalized\ RMSE = \frac{RMSE}{Range\ of\ F_i} \times 100\% \tag{5.6}$$

$$R^2 = [1 - \frac{\sum_{i=1}^{N}(y_i - \hat{y}_i)^2}{\sum_{i=1}^{N}(y_i - \bar{y}_i)^2}] \times 100\% \tag{5.7}$$

The relative error in the estimate was given with a normalized RMSE of 0.1808% and the coefficient of determination, $R^2$ 99.98% for the 13mm configuration of five sensors. For the 22mm configuration of five sensors, the RMSE is found to be 0.5138% and the $R^2$ is 99.86%. This also gives us some statistics to improve the estimation using a probabilistic sensor model. The least square error (RMSE) and $R^2$ of the contact force is used as the same formulation as in [48]. It has also considerable accuracy compared to the systems described in [48] where the similar z-axis normalized RMSE and $R^2$ were found to be respectively 1.17% and 99.78%.

## 5.3 Verification of Contact Pressure Points Model

Fig. 5.7 shows the contact force distribution among the five sensors placed beneath the feet for an application of 30N force in total to the symmetric 24mm padded humanoid foot and about 23N

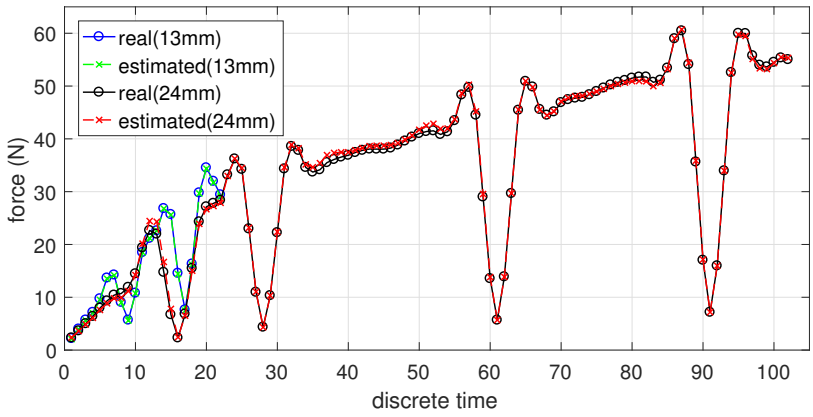


Figure 5.6: Contact force estimation and accuracy plot.

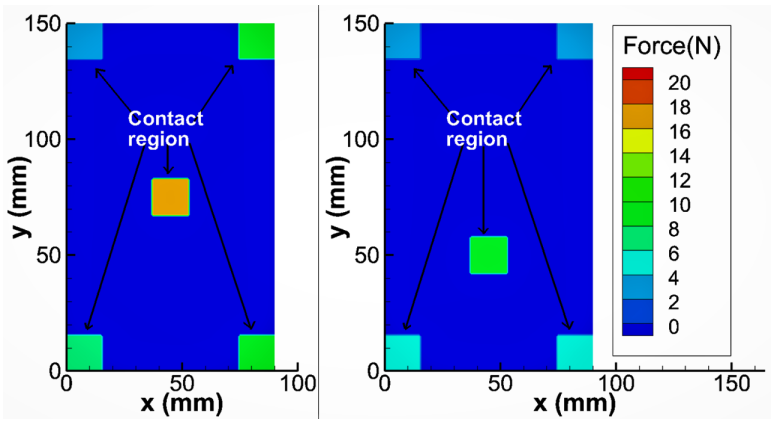


Figure 5.7: Contact force distribution among the five sensors using the proposed contact model in symmetric (left) and asymmetric (right) humanoid foot.

in total to the asymmetric foot. It is visible that a significant amount of force is applied in the middle sensor in both cases which verifies the pressure point modeling described in section III. The contact region is defined by the design to be $15 \times 15$ mm squares indicated.

## 5.4 ZMP measurement

The objective of the ZMP experiment is to observe the system noise in ZMP measurement and see how closely the sensors measure the ground truth reference ZMP generated in the system.

For conducting the ZMP measurement experiment, a reference CoM trajectory is generated using a linear inverted pendulum motion (LIPM) from the ankle actuators in ATHENa visible in Fig. 4.7(a). Then equation (3.17) is used to collect the ZMP data from two separate configurations of using the traditional four contact point model and our proposed five contact point model (Fig. 5.8). To make it coincidental with the CoM trajectory, some slow motion of the CoM is generated with an amplitude of 30mm in the foot projection around the center of the base of leg. An abrupt motion is deliberately introduced at the beginning of the trajectory to observe the response of both systems to it. The proposed contact model produces less vibrations as it has more contact area. It reaches to the RMSE value difference of the reference trajectory in 65 samples earlier than the four contact point system. The proposed system also exhibits quite accurate measurement to the ground truth reference trajectory that is visible in Fig. 5.8a. This experiment verifies that the system can be used as a robust system for ZMP estimation. The results are affected by small oscillations which is due to the structural vibrations in the system as well as fractions of millimeters difference in elastomer padding that causes unevenness in the ground contacts. This difference can only be alleviated by industrial grade manufacturing of the molding of elastomer.

Fig. 5.9 shows the ZMP comparison between the two configuration of 5 sensors and 4 sensors. The deviation is caused by the deliberate disturbance introduced at the start of the ZMP estimation experiment. The RMSE of both of the deviation was measured to be 7.91mm and 11.182 respectively for the 5 sensor and 4 sensor configuration. It is noteworthy that this RMSE is not an actual error of the ZMP estimation but merely a measurement of deviation from the reference trajectory

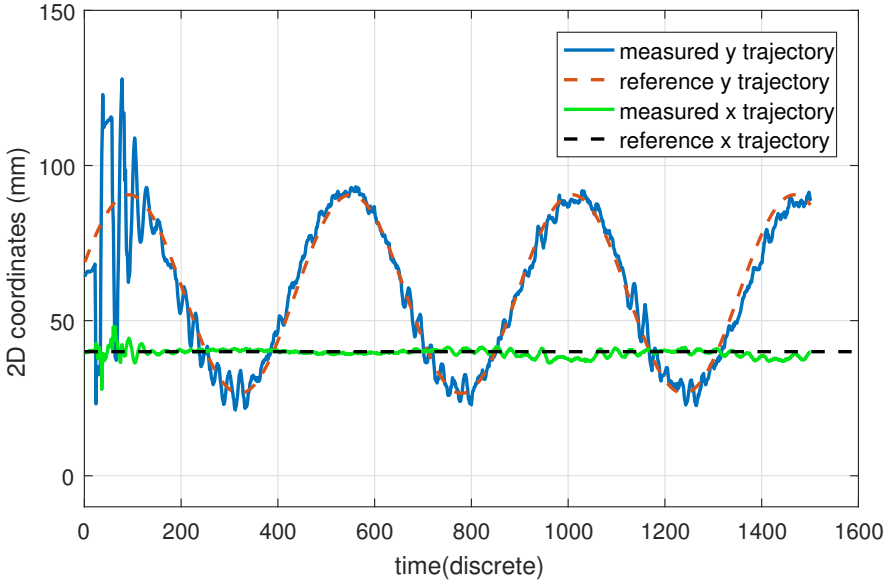


(a)

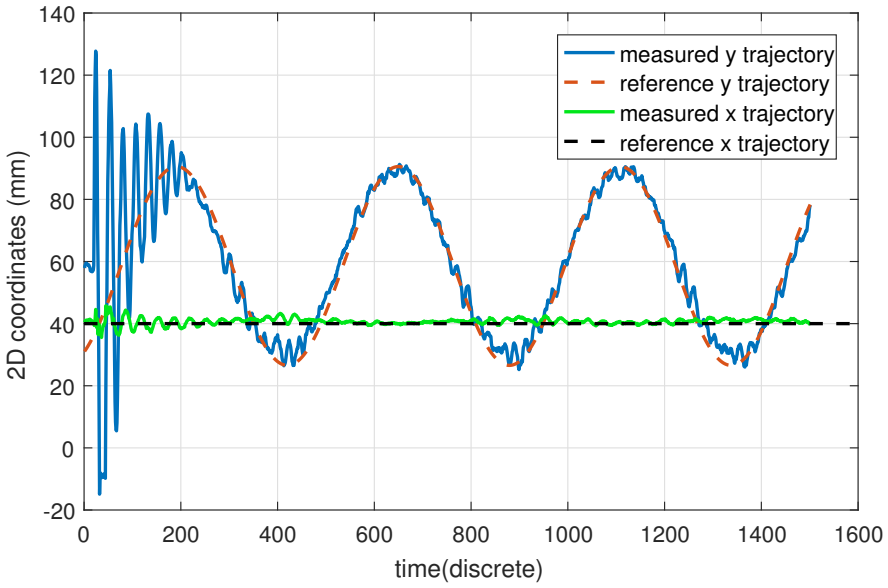


(b)

Figure 5.8: Reference ZMP trajectory vs measured ZMP trajectory of the footplate showing in both x and y axis. (a) results using 5 sensor configuration (b) results using 4 sensors, turning off the middle sensor.

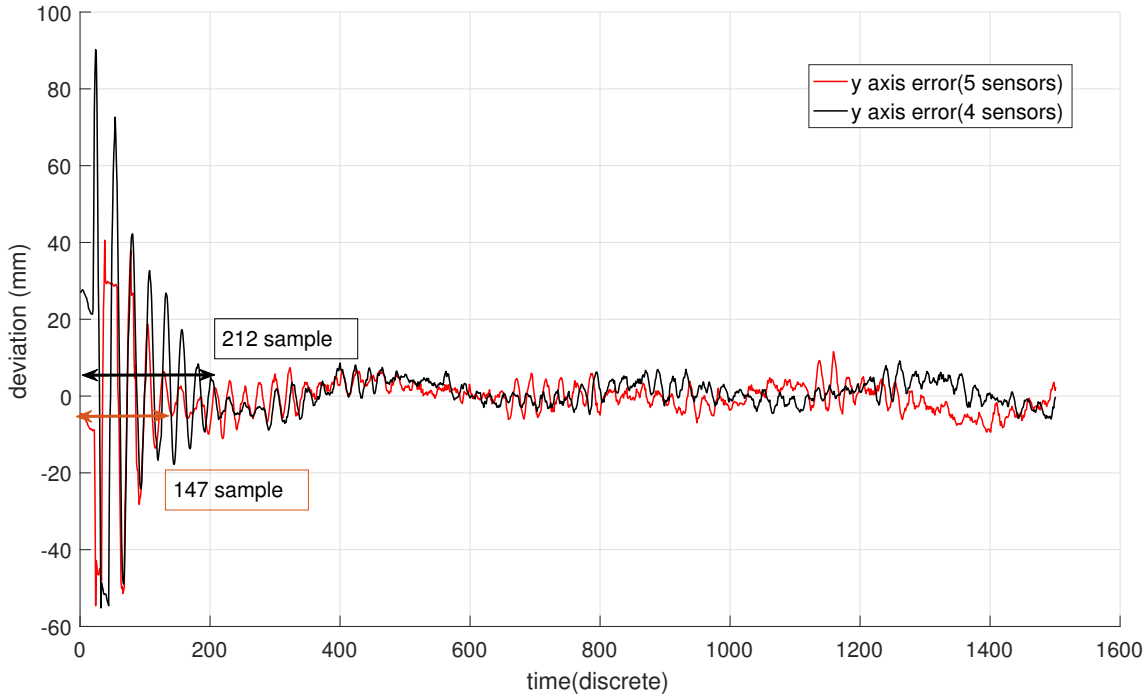


Figure 5.9: Deviation of ZMP from reference for 5 sensor and 4 sensor configuration

due to the disturbances and motion generated vibrations. This is a negative effect of the compliant foot system having soft interface with the ground. The RMSE of both the systems are approximately 3mm at steady state which can be eradicated using appropriate Kalman filtering with the ZMP motion model. For example, the steady state noise is maximum where there is a change in direction of velocity in the point mass system. An appropriate motion model would incorporate this experimental data to eradicate this noise using Recursive Bayesian Estimation (RBE) technique. After that the ZMP data can be used for the whole body control of the humanoid.

## 5.5 3 Axis Force Measurement

In this experimentation, a different approach of ANN regression than the previous one is used. The previous individual models were helpful for having high accuracy in z-axis force and ZMP but incapable of estimating 3-axis force . The architecture of the ANN has to be changed to a Multiple Input Multiple Output(MIMO) system for estimating the 3 axis forces. By training the neural network, the system transfer function of the foot sensor is approximated over particular regions of the state space. This creates a mapping that encompasses the non-linearity between the sensor output and the multi-axis force data. Lu et al. has explored using ANN for strain gauge to force/torque calibrations [68]. It offers the advantages of only requiring a one-time calibration procedure and is able to provide force feedback to the system in real- time.The overall algorithm is explained in Fig. 5.10. This also requires a more rigorous experimentation with commercial multi axis force sensor as the ground truth for estimation. A 3-axis commercially available Varience force sensor is used with a custom made testbed for data collection and validation. The experimental setup is shown in Fig. 5.11.

The five analog voltages are assembled into an array where $v_{n,i}$ represents the n-th voltage sample

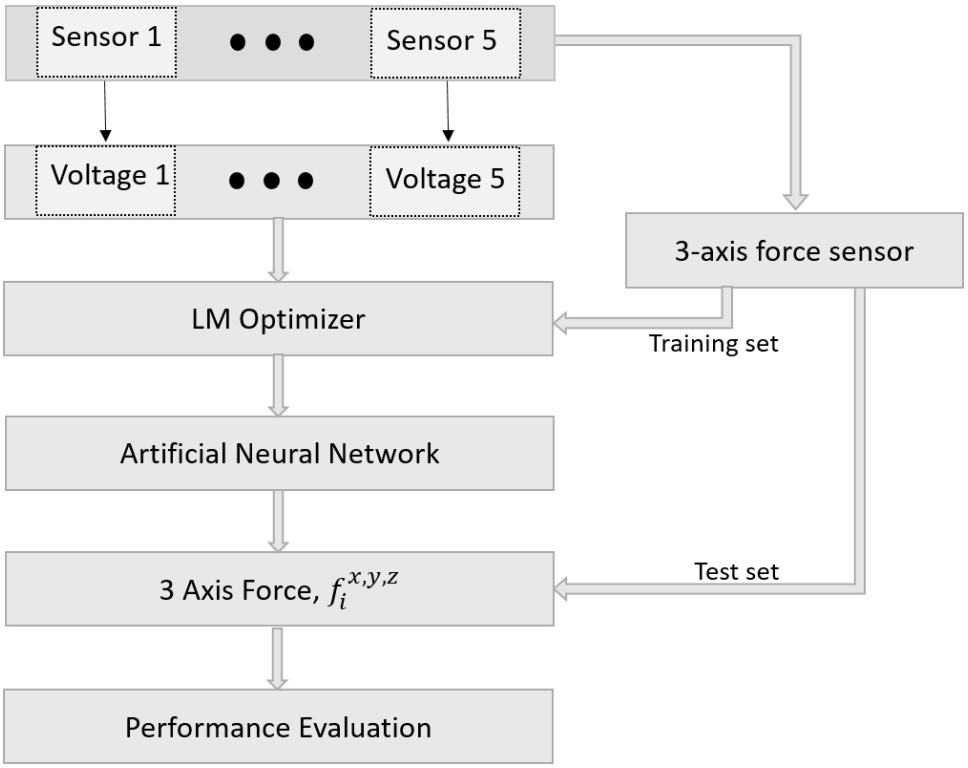


Figure 5.10: Algorithm of fitting sensor data into neural network for 3-axis force estimation.

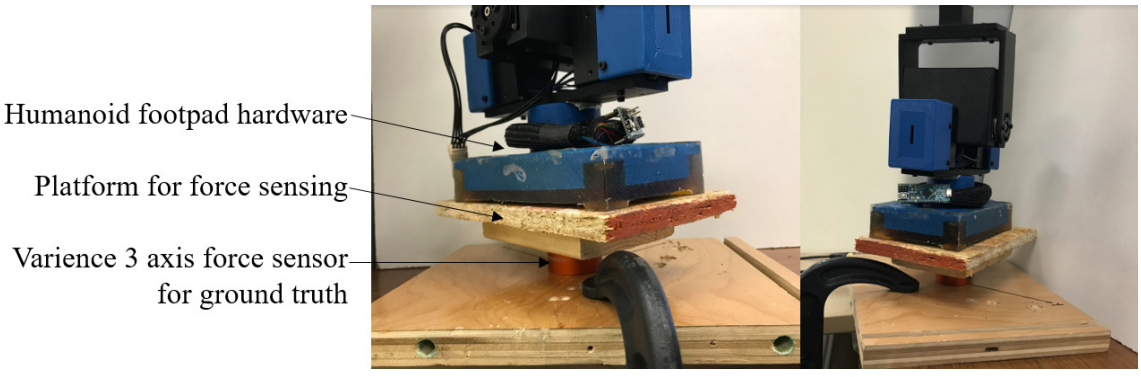


Figure 5.11: Experimental Setup for 3-axis force estimation.

from the $i-th$ pressure sensor. Here $i \in (1...5)$ and $n \in (1,...,N)$.

$$V = \begin{bmatrix} v_{1,1} & \cdots & v_{1,i} & \cdots & v_{1,5} \\ \vdots & \ddots & \vdots & \ddots & \vdots \\ v_{n,1} & \cdots & v_{n,i} & \cdots & v_{n,5} \\ \vdots & \ddots & \vdots & \ddots & \vdots \\ v_{N,1} & \cdots & v_{N,i} & \cdots & v_{N,5} \end{bmatrix} \tag{5.8}$$

The loading conditions on the footpad are measured by the multi axis force sensor and can be represented as

$$F(t) = [F_x(t) \;\; F_y(t) \;\; F_z(t)]^T \tag{5.9}$$

where $F_j(t)$ is the recorded force in each respective axis. This change in voltage output from sensors due to the pressure distribution, V(t) is then parsed in MATLAB$^{TM}$ and the pressure distribution and the applied forces are empirically correlated. A feed-forward neural network is created where an input-output relationship is mapped between the pressure distribution as measured by the five barometric pressure sensors and the 3 axis forces recorded by the F/T sensor. The Levenberg-Marquardt optimization network training function [69] then uses a back-propagation algorithm to update the weights and bias values of the neural network until the minimum mean squared error is obtained and the desired performance is realized. The Levenberg-Marquardt algorithm is given as:

$$[J^T W J + \lambda diag(J^T W J)]\delta = J^T W[F(t) - \hat{F}(t)] \tag{5.10}$$

where $J$ is the Jacobian matrix, $W$ is the weighting matrix, $\lambda$ is the algorithmic parameter, $\delta$ is the increment in each iteration, F(t) is the target force output from the F/T sensor and on the use of artificial neural networks for force sensing $\hat{F}(t)$ denotes the force estimates of the ANN. This method is based on work done by Ananthanarayanan et al. [66]. The LM optimizer indicated very good correlation between the output and target values which is a metric of the suitability of the neural network regression technique. Fig. 5.12 represents the $R^2$ plot of the process. The three plots represent the training, validation, and testing data. The dashed line in each plot represents the perfect result – outputs = targets. The solid line represents the best fit linear regression line between outputs and targets. The $R^2$ value is an indication of the relationship between the outputs

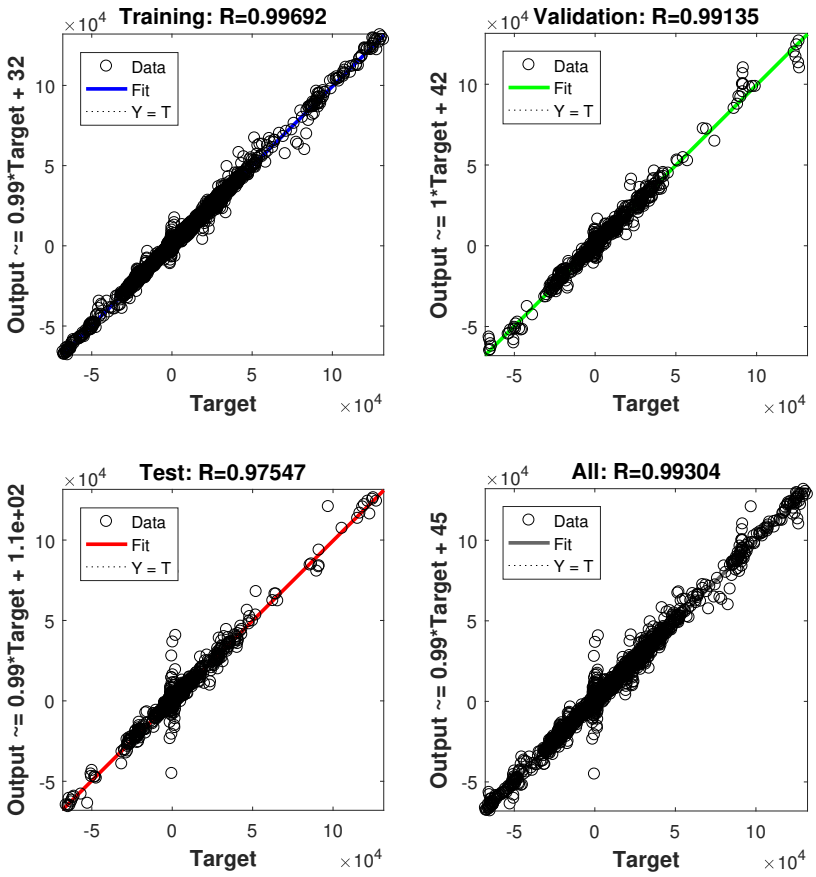


Figure 5.12: Coefficient of Determination graph of training, validation and testing using the LM optimizer.

and targets.

However, the LM optimizer did not produce satisfactory accuracy and using MATLAB required much high convergence time. Therefore, the scikit-learn library [70] has been utilized with an LBFGS optimizer with resulted in much better accuracy. A network with two hidden layers were used with 200 and 100 nodes in the first and second layers respectively. An adaptive learning rate was undertaken with rectified linear unit function as the activation function and LBFG-S as the optimization algorithm.

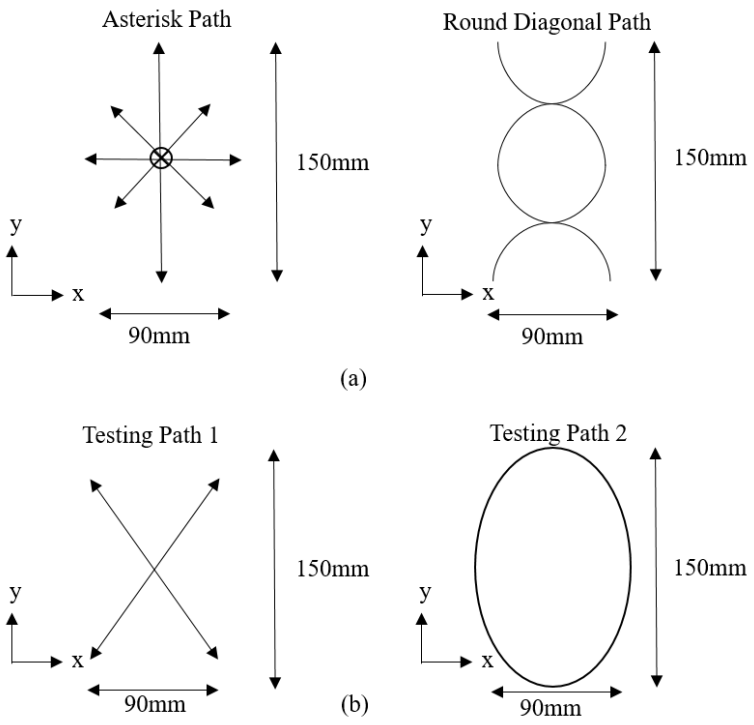


Figure 5.13: Training and testing paths used to collect the data needed for the ANN. The furthest points on each sub-trajectory correspond to the amplitude of the sinusoidal LIPM motion. (a) Training Paths (b) Testing Paths.

Then various training and testing paths have been defined using both LIPM motion and manual force application in the direction of all three axis. The overall training and testing paths are show in Fig. 5.13.

The data collection process has been automated in this step through serial connection to the sensor system and also the commercial sensor for ground truth. The simultaneous read operation has been performed in MATLAB ad data has been parsed according to equation 5.8. In each axis, 2000 samples have been collected through repeatedly applying pressure in all of the three axis in in different combinations.

The results were obtained using several different test procedures. The data collected has a large range of variations for it to get a nice fit without much overfitting and underfitting. A 10% cross validation ratio was kept while training the networks to evaluate overfitting.

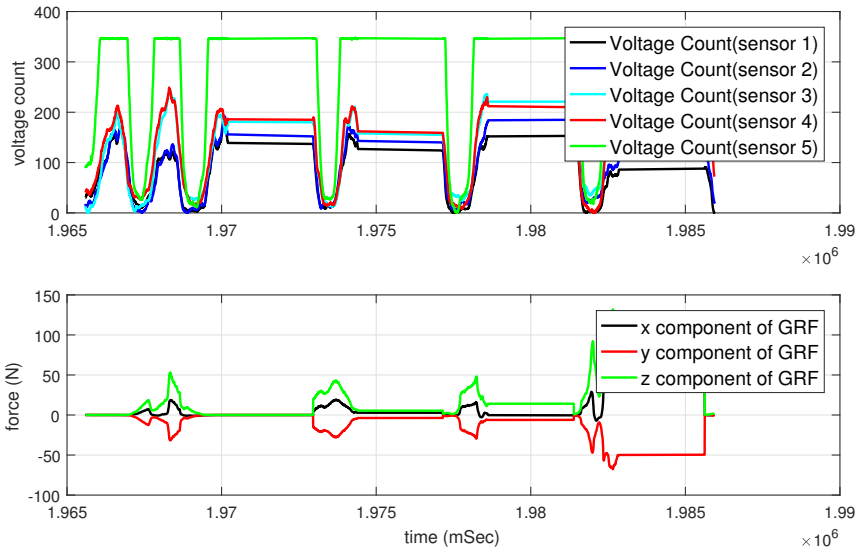


(a) Footpad sensor voltage counts and force sensor readings in the Z-axis using manual force application

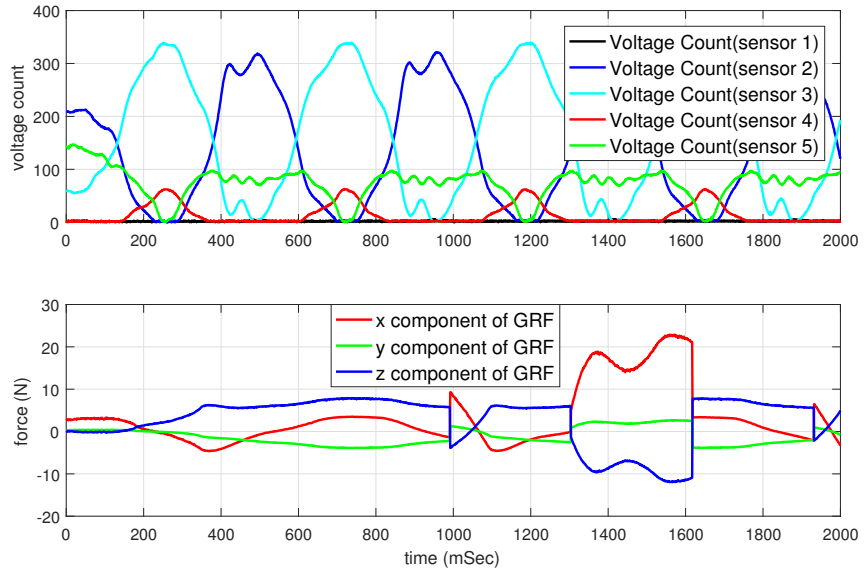


(b) Footpad sensor voltage counts and force sensor readings in the Y-axis using manual force application

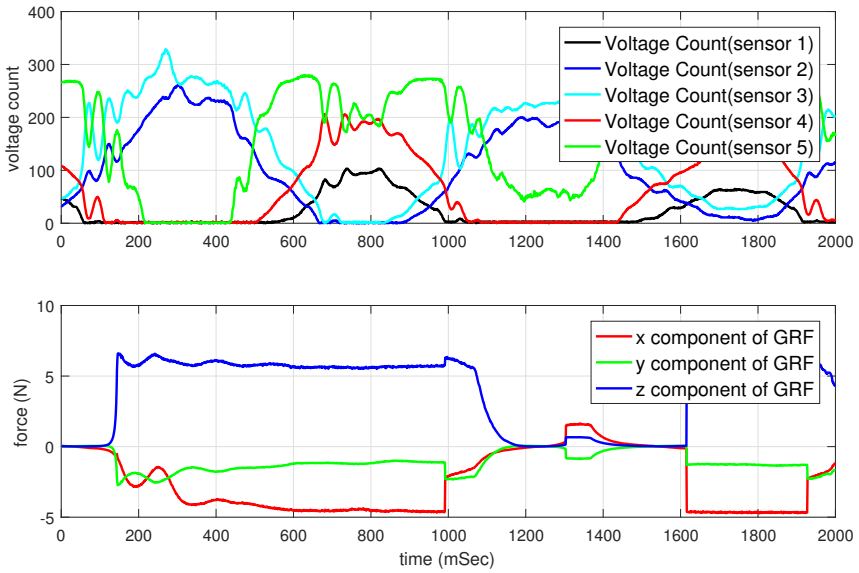


(c) Footpad sensor voltage counts and force sensor readings in the X-axis using manual force application

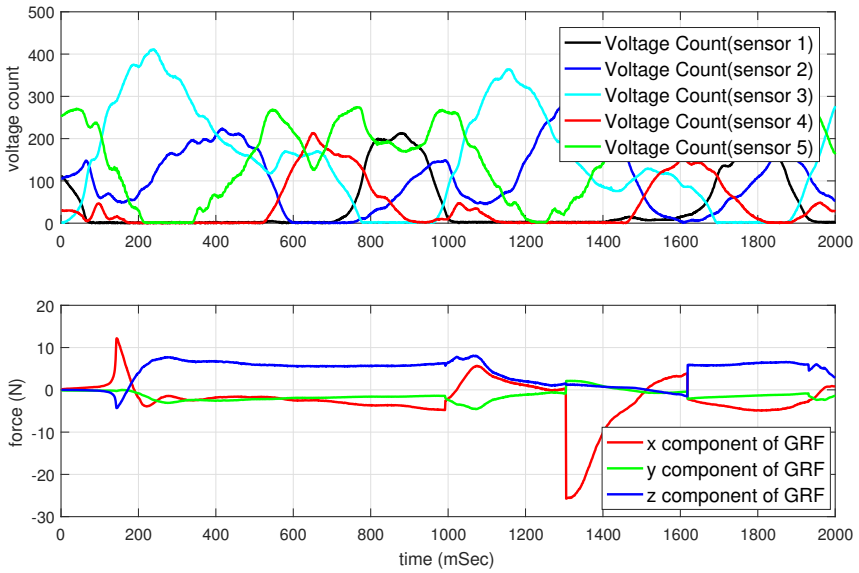


(d) Footpad sensor voltage counts and force sensor readings in the round diagonal training path using LIPM motion

Figure 5.14: Footpad sensor voltage counts and force sensor readings. Data collected for the multivariate ANN regression.

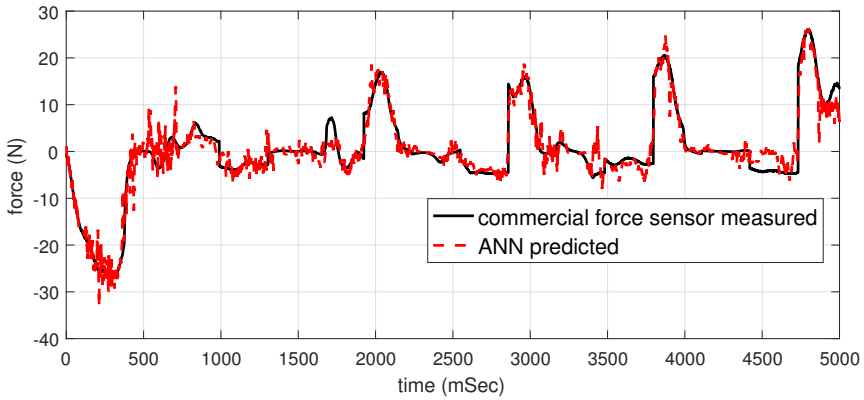


(a) Predicted vs Measured Forces in the X-Axis

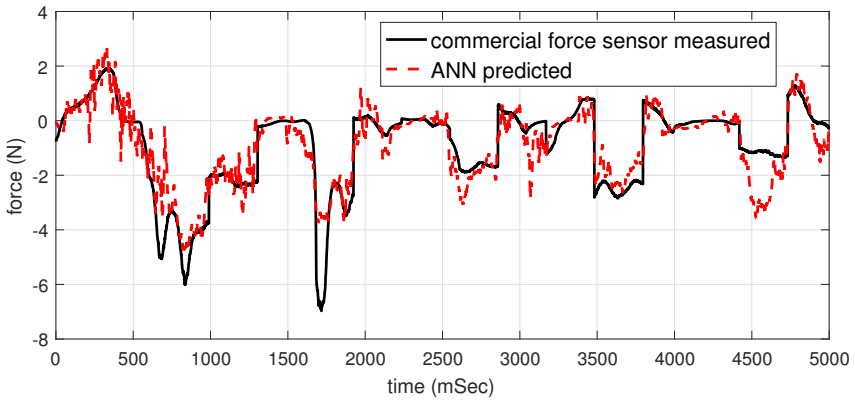


(b) Predicted vs Measured Forces in the Y-Axis

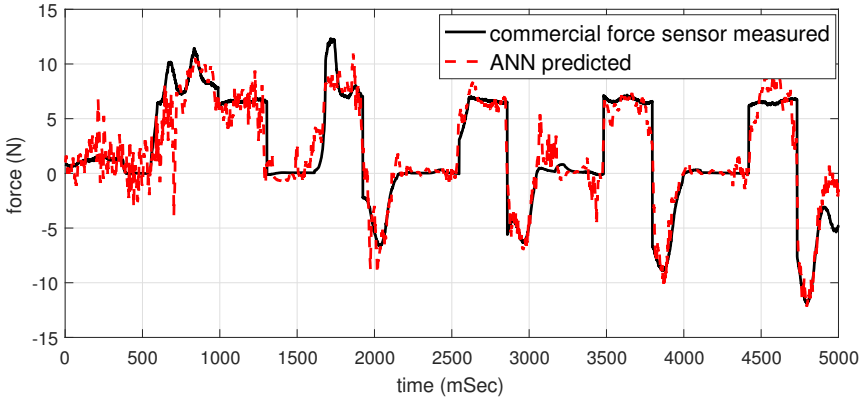


(c) Predicted vs Measured Forces in the Z-Axis

Figure 5.15: Experimental results for agreement between the predicted force and actual force. The black line shows the actual force measured and the red line shows the ANN2 predicted force.

Table 5.2: Comparative performance evaluation using RMSE, Normalized RMSE, And the Coefficient of Determination, $R^2$ for each axis

| Z-axis | RMSE | Normalized RMSE (%) | $R^2$ |
|---|---|---|---|
| ATHENa (ANN1) | 0.5138 | 0.345 | 99.86 |
| ATHENa (ANN2) | 3.47 | 14.37 | 87.7 |
| MIT Cheetah | 2.42 | 1.17 | 99.90 |
| Y-axis | | | |
| ATHENa | 1.64 | 18.54 | 76.63 |
| MIT Cheetah | 12.63 | 10.14 | 79.02 |
| X-axis | | | |
| ATHENa | 5.3723 | 10.17 | 83.62 |
| MIT Cheetah | 10.48 | 8.30 | 81.03 |

The results are collected and compared with the system developed by Chuah et al [48]. It is summarized in Table 5.2. In the end a data set of 15000 samples were used for training the neural network and 4000 samples for testing it. The results indicate reasonable accuracy in x and y axis compared to the similar system by Chuah et al. However, this particular regression technique has a poor estimation of the normal forces. This issue can be bypassed by ignoring the z-axis estimate from this regression model and use the model for ZMP estimation for the normal force estimation. Therefore, only the MIMO system is used to measure the x and y axis forces acting upon the footpad.

The error histogram is also presented to showcase the multi axis force estimators performance. It is shown in Fig. 5.16. The histogram shows the error for 4000 data points in 3 axis, therefore a total of 12000 data points. It is visible that more than half of that has an error of 0.23 . The histogram plots 20 bins which shows very small amount of samples having high percentage of error in the test data.

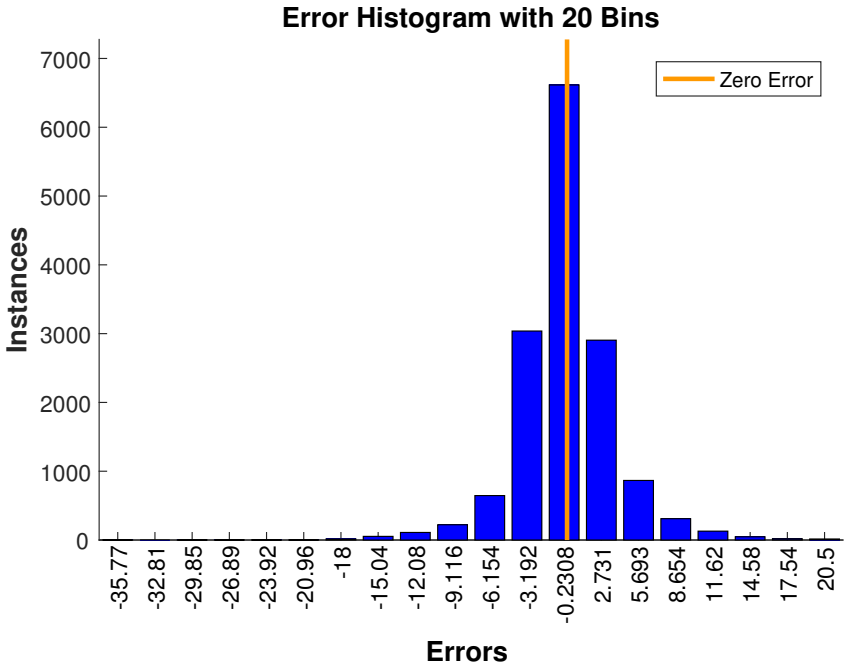


Figure 5.16: Error histogram of the proposed multi-axis force estimator.

## 5.6 Preliminary Analysis of Stress/Strain on Compliant Foot

Foot is the most stressful part of the robot as it endures all the weight and impact force of the robot. The mechanical vibrations are caused by the deformation of joints which experience high directional force, specially in the z direction. The deformations can cause instability in agile motion of robot as well as degradation of structure and at certain point it can also lead towards breakdown. Moreover, in the specific system of current study it can cause connection issues in the electronic system for the embedded sensors. For all of these reasons, a formal stress-strain analysis is of great importance for the design procedure of soft foot.

In this study, a stress versus deformation study is presented for the proposed system consisting of conventional foot contact point model. The analysis is done in COMSOL Multiphysics software using FEM and model building library. The structural mechanics module provides great tools for analyzing this system and compare different configurations for better structural performance. The lesser the deformation, the more stable and better performing the system becomes.

The total Lagrangian formulation is used for structural analysis in COMSOL Multiphysics for both small and finite deformations . This assumes that the computed stress and deformation state is always referred to the material configuration, rather than to current position in space. In addition, material properties are always given for material particles and with tensor components referring to a coordinate system based on the material frame. The gradient of the displacement is always computed with respect to material coordinates, which happens quite frequently in the following theory. The displacement or deformation gradient in 3D is referred to by $u = [u, v, w]$.

$$\nabla u = \begin{bmatrix} \frac{\delta u}{\delta X} & \frac{\delta u}{\delta Y} & \frac{\delta u}{\delta Z} \\ \frac{\delta v}{\delta X} & \frac{\delta v}{\delta Y} & \frac{\delta v}{\delta Z} \\ \frac{\delta w}{\delta X} & \frac{\delta w}{\delta Y} & \frac{\delta w}{\delta Z} \end{bmatrix} \tag{5.11}$$

The total strain tensor is written in terms of the displacement gradient

$$\varepsilon = \frac{1}{2}(\nabla u + \nabla u^T) \tag{5.12}$$

The Duhamel-Hooke's law relates the stress tensor to the strain tensor and temperature:

$$s = s_0 + C : (\varepsilon - \varepsilon_0 - \alpha\theta) \tag{5.13}$$

where $C$ is the 4th order elasticity tensor, ":" stands for the double-dot tensor product (or double contraction), $s_0$ and $\varepsilon_0$ are initial stresses and strains, $\theta = T - T_{ref}$, and $\alpha$ is the thermal expansion tensor.

Under the assumption of small displacements, the normal strain components and the shear strain components are related to the deformation as

Table 5.3: Properties of Materials used in FEA

| Material | Young's Modulus (MPa) | Poisson's Ratio (no unit) | Density (Mg/m3) | Tensile Strength (MPa) |
|---|---|---|---|---|
| ABS Plastic (20% infill) | 1000 | 0.33 | 0.25 | 16 |
| Vytaflex-20 | 5 | 0.5 | 1.02 | 1.379 |

$$\begin{aligned} \varepsilon_x &= \frac{\delta u}{\delta x} \qquad & \varepsilon_{x,y} &= \frac{1}{2}(\frac{\delta u}{\delta y} + \frac{\delta v}{\delta x}) \\ \varepsilon_y &= \frac{\delta v}{\delta y} \qquad & \varepsilon_{y,z} &= \frac{1}{2}(\frac{\delta v}{\delta z} + \frac{\delta w}{\delta y}) \\ \varepsilon_z &= \frac{\delta w}{\delta z} \qquad & \varepsilon_{z,x} &= \frac{1}{2}(\frac{\delta u}{\delta z} + \frac{\delta w}{\delta x}) \end{aligned} \tag{5.14}$$

For a general anisotropic linear elastic material and in the case of plane stress, COMSOL solves three equations $s_{i3} = 0$ for i3 with $i = 1,2,3$, and uses the solution instead of Equation 5.12 for these three strain components. It is to be noted that for an isotropic material, only the normal out-of-plane component $\varepsilon_{33}$ needs to be solved for.

The Young's modulus and Poisson's Ratio is used as the modulus of elasticity and other material properties of the materials used for manufacturing are specified using existing study of these properties. The two materials used are ABS plastic for 3D printed foot skeleton and Vytaflex 20 elastomer for footpad. A 20% infill is used for the printing with ABS plastic and the properties are calculated based on the work done by Dudescu et al. [71]. The elastomer properties has been cross referenced by the materials data book and the Vytaflex-20 technical specifications . The table below lists the properties used for these two materials.

The results of the FEA shows significant improvement in decreasing the deformations due to the addition of the fifth sensor. The deformation due to the application of 100 N and 1000N total stress on the foot base plane is shown for the conventional 4 sensor configuration in Fig. 5.17 and for the proposed system in Fig. 5.18. The deformation maintains a linear relationship with

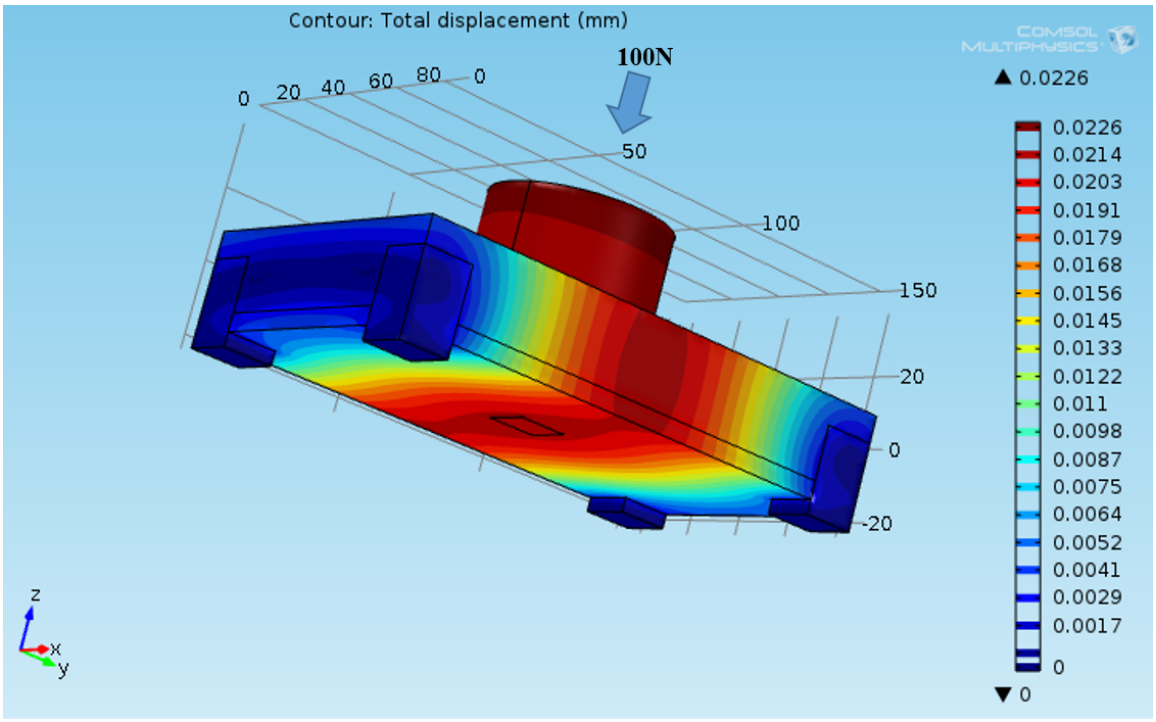


(a) Deformation of compliant foot in contours with 100N force applied at the base.

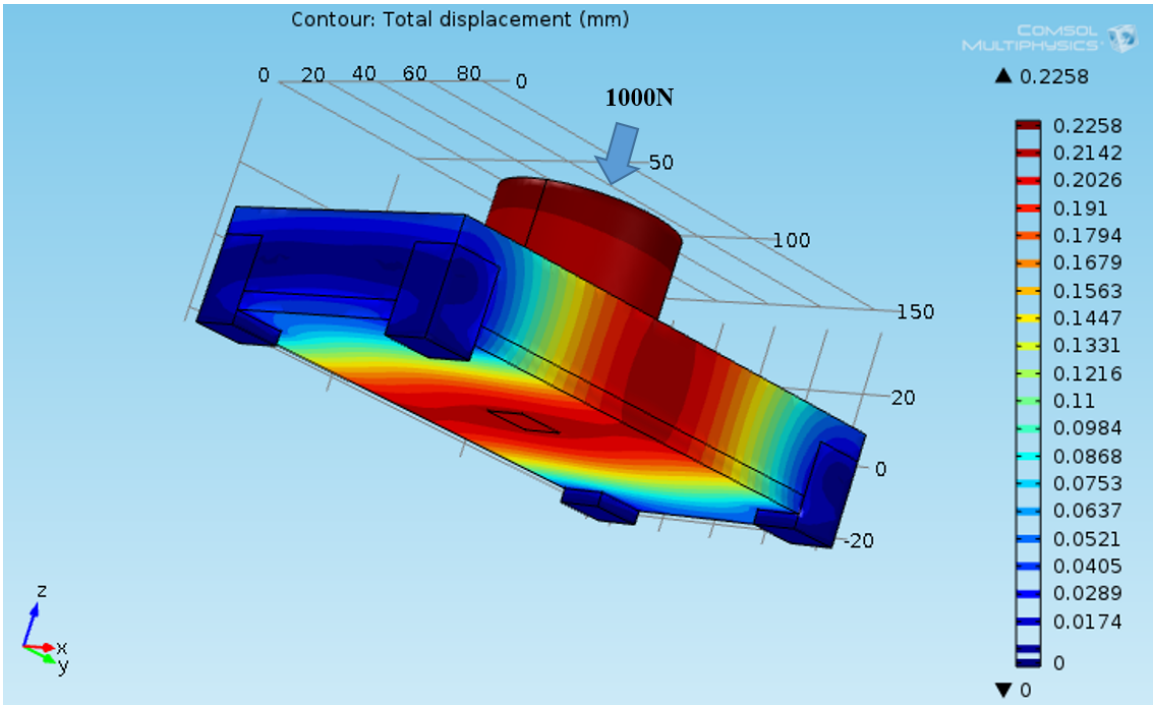


(b) Deformation of compliant foot in contours with 1000N force applied at the base

Figure 5.17: FEA of compliant foot with conventional 4 sensor configuration. A plane stress in applied in the negative z-axis on the foot base plane to simulate the humanoid loading on the foot.

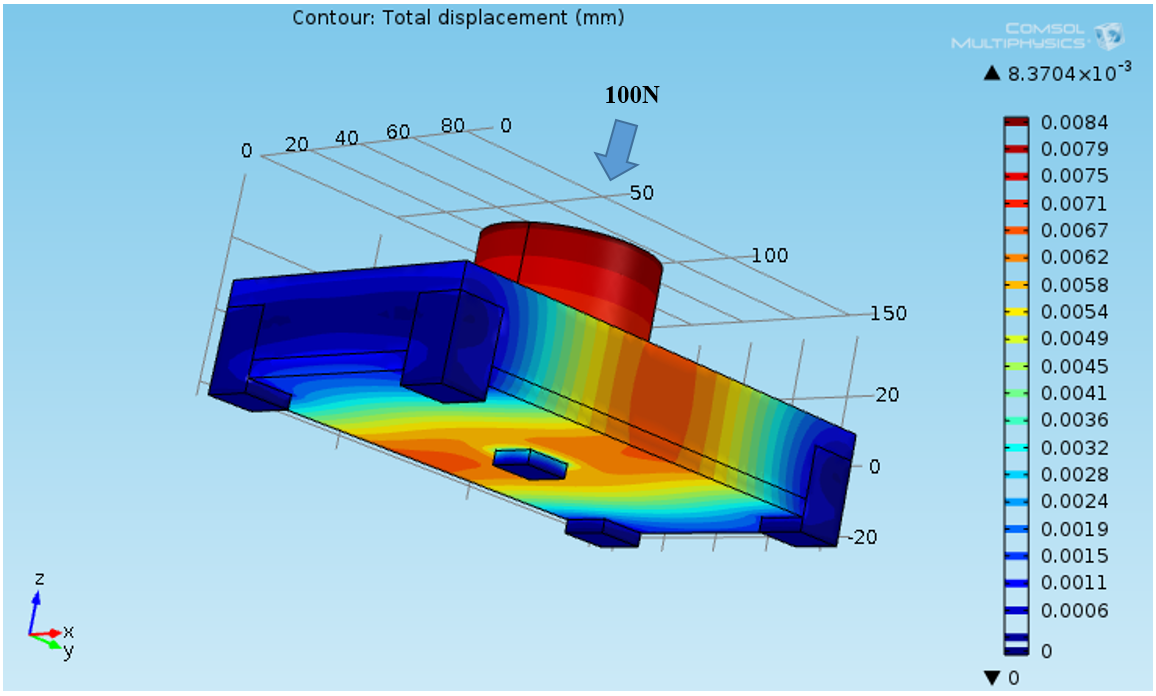


(a) Deformation of compliant foot in contours with 100N force applied at the base.

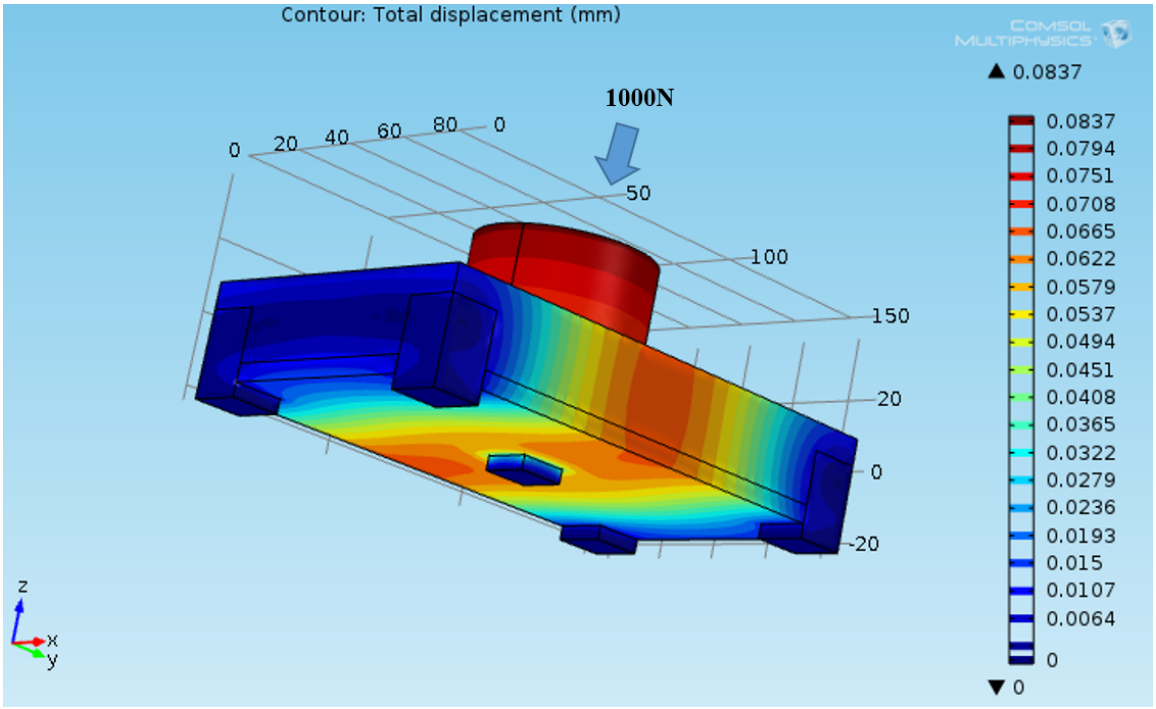


(b) Deformation of compliant foot in contours with 1000N force applied at the base

Figure 5.18: FEA of compliant foot with our proposed 5 sensor configuration.

the applied stress. However, the noteworthy point is that the proposed system shows three times less deformation from the conventional configuration. This can be considered as a significant design performance metric of the proposed soft foot that can lead to stable and reliable motion of humanoids.

# Chapter 6

# Conclusions

In this final chapter, all the results are discussed and the important findings are duly noted. As this work is a new approach towards GRF and ZMP measurement for full scale humanoids, there are many areas to improve which is also discussed in details. The final remarks emphasize how the objectives has been achieved and the systems effectiveness towards a robust footpad system in humanoid robots.

## 6.1 Discussion And Future Works

The ultimate goal of this system is to have a holistic way of measuring GRF and associated ZMP as well as introducing soft but high friction footpad for compliant motion of humanoids. The structural design also focuses on minimal addition of hardware via efficient integration of sensors and have adjustable design parameters. It can be an alternate to the expensive F/T sensors while being more lightweight, immensely cheaper and eradicating the inertial noise. The range can however be made much higher than our current capability of 170 N by either increasing the elastomer padding or using different material as used in [30]. Moreover, the cost can be further reduced by building the system from chip level, not using off-the-shelf Takktile systems. The primary achievements and characteristics of our proposed system are shown in table 6.1 where the specifications are taken from industrial grade F/T sensor specifications.

Table 6.1: Sensor System performance

| Feature | F/T sensor system (high range) | F/T sensor system (low range) | Our system |
|---|---|---|---|
| Range of operation | 1700 N | 290 N | 170 N |
| Weight | 1 kg | 0.6 kg | 0.4 kg |
| Resolution | 0.29 | 0.06 | 0.06 |
| Cost | $10000-$25000 | $5000-$8000 | $200-$500 |

There is however several areas to improve and further study. Introducing some auto-calibration mechanism can increase the user-friendliness greatly. Moreover, to utilize the maximum speed of the $I^2C$ channel, a dedicated microcontroller and additional Analog-to-Digital Converter (ADC) would be used in future prototypes. Thus it would be able to directly process the voltage signals from the barometric pressure sensor array on-board and send out the predicted multi-axis forces. This could be done with SPI communications for high bandwidth. Other technologies of force sensing can also be explored that can generate this accuracy with greater range. The five sensor configuration is the proposed basic layout for effectively measuring the foot contact force and ZMP.

Collecting additional training data may further fine-tune the ANN parameters and will allow us to minimize the errors in the force sensing. Only a few trajectories, repeated at varying normal loads, was used to produce the current correlation. There might be some load history dependence (e.g. stress relaxation and hysteresis) which needs to be investigated further. Specifically, impact tests may prove to be the most relevant training method for agile motion and would provide more telling information.

In order to further improve the measurement of shear forces, the number of sensors and alternative placement of the barometric pressure sensors is currently being further explored. Rather than having the pressure sensors spaced regularly, an irregular spatial arrangement or circular orientation may increase sensitivity and accuracy to shear forces. The minimum number of sensing elements that is needed to detect forces in three axes is being investigated in hopes of reducing

the overall footprint. Moreover, a combination of pressure sensors with different sensing ranges could be used together in a single footpad to achieve a greater dynamic range in force measurement. In the human skin, there are four main types of mechanoreceptors (i.e. Ruffini's end organs, Meissner's corpuscles, Pacinian corpuscles and Merkel's discs). These mechanoreceptors each perform a different role, enabling the skin to differentiate between a wide variety of forces and textures [72]. By varying the pressure range and types of the barometric pressure sensors used in the sensor array, as well as the material properties of the elastomer, a similar effect can be achieved.

Furthermore, an extended study has to be conducted with the number of sensors and alternative placement under the feet. A higher number of sensors with appropriate modeling can lead the robot to handle uneven terrains with the possibility of generating an estimate of the terrain surface and more precise multi-axis force/torques. Finally, a combination with the existing optimized soft sole research can be integrated with the mold design as our system highly flexible for any kind of modification and designed with the multiple purpose of shock absorption too for humanoids.

## 6.2 Conclusion

Agile walking motion of humanoid robots places large forces instantaneously on the footpad introducing undesirable effects such as inertial noise as well mechanical shock on the whole body circulated from the feet contact. The robot also need to measure the forces and ZMP very precisely from that contact. Current sensors are not able to mitigate these issues while giving an accurate measurement. This research presents a footpad with integrated force sensing capabilities that addresses these issues in ground locomotion. Ground reaction forces can be accurately measured during ground locomotion, allowing a robot to react to changing terrain and incipient slip. The foot is made of a polyurethane elastomer with an embedded cluster of barometric pressure sensors, which permits normal and shear forces to be measured in a roundabout way without the need to uncover the sensor. The configuration of sensors is derived from a pragmatic approach of humanoid footpad pressure point modeling. The elastomer deposition beneath the pressure sensors gives strength under repeating impacts while as yet being sufficiently agreeable to offer considerable

traction. A one-time training process implemented using an artificial neural network is sufficient to relate the 3-axis forces with the feet sensor outputs. The multi-axis feet sensor is able to detect normal forces to the extent of 170N with an RMSE of 0.18% and upto 50N in the X and Y axis with an RMSE of 10.1% and 14.64% respectively in the experimental setup carried out. All in all, the system is a lightweight ($<$ 400g) and low cost ($<$ \$400), robust yet strikingly adjustable foot-pad sensor suitable for use in legged humanoids performing locomotion to detect the occurrence of ground contact and the ground reaction forces involved.

# Bibliography


[1] S. Kajita, H. Hirukawa, K. Harada, and K. Yokoi, *ZMP and Dynamics*. Berlin, Heidelberg: Springer Berlin Heidelberg, 2014, pp. 69–103. [Online]. Available: https://doi.org/10.1007/978-3-642-54536-8_3

[2] K. Kappaganthu and C. Nataraj, "Optimal biped design using a moving torso: Theory and experiments," in *Biped Robots*, A. C. P. Filho, Ed. Rijeka: IntechOpen, 2011, ch. 3. [Online]. Available: https://doi.org/10.5772/13791

[3] G. Humphry, *The human foot and the human hand*. Macmillan, 1861. [Online]. Available: https://books.google.co.ao/books?id=SJIZAAAAYAAJ

[4] S. Davis and D. G. Caldwell, "The design of an anthropomorphic dexterous humanoid foot," in *2010 IEEE/RSJ International Conference on Intelligent Robots and Systems*, Oct 2010, pp. 2200–2205.

[5] L. Klenerman, B. Wood, and N. L. Griffin, *The human foot a companion to clinical studies*. Springer-Verlag London Limited, 2006.

[6] M. T. Francomano, D. Accoto, and E. Guglielmelli, "Artificial sense of slip—a review," *IEEE Sensors Journal*, vol. 13, no. 7, pp. 2489–2498, July 2013.

[7] Q. Liang, D. Zhang, G. Coppola, Y. Wang, S. Wei, and Y. Ge, "Multi-dimensional mems/micro sensor for force and moment sensing: A review," *IEEE Sensors Journal*, vol. 14, no. 8, pp. 2643–2657, 2014.

[8] K. Kaneko, K. Harada, F. Kanehiro, G. Miyamori, and K. Akachi, "Humanoid robot hrp-3," in *Intelligent Robots and Systems, 2008. IROS 2008. IEEE/RSJ International Conference on*. IEEE, 2008, pp. 2471–2478.

[9] J. Englsberger, A. Werner, C. Ott, B. Henze, M. A. Roa, G. Garofalo, R. Burger, A. Beyer, O. Eiberger, K. Schmid, *et al.*, "Overview of the torque-controlled humanoid robot toro," in *Humanoid Robots (Humanoids), 2014 14th IEEE-RAS International Conference on*. IEEE, 2014, pp. 916–923.

[10] S.-J. Yi, S. G. McGill, L. Vadakedathu, Q. He, I. Ha, J. Han, H. Song, M. Rouleau, B. Zhang, D. Hong, M. Yim, and D. Lee, "Team thor's entry in the darpa robotics challenge trials 2013," *Journal of Field Robotics*, vol. 32, 12 2014.

[11] C. Knabe, J. Seminatore, J. Webb, M. Hopkins, T. Furukawa, A. Leonessa, and B. Lattimer, "Design of a series elastic humanoid for the darpa robotics challenge," in *Humanoid Robots (Humanoids), 2015 IEEE-RAS 15th International Conference on*. IEEE, 2015, pp. 738–743.

[12] H.-o. Lim and A. Takanishi, "Biped walking robots created at waseda university: Wl and wabian family," *Philosophical transactions. Series A, Mathematical, physical, and engineering sciences*, vol. 365, pp. 49–64, 02 2007.

[13] I. Kato, "Development of wabot 1," p. 173–214, 1973.

[14] F. M. Y. T. I. K. Katoh, I and Y. Nakano, "Development of legged walking robots," vol. 68, no. 10, pp. 25–30, 1986.

[15] A. Sano and J. Furusho, "Control of torque distribution for the blr-g2 biped robot," in *Fifth International Conference on Advanced Robotics 'Robots in Unstructured Environments*, June 1991, pp. 729–734 vol.1.

[16] K. Hirai, M. Hirose, Y. Haikawa, and T. Takenaka, "Development of honda humanoid robot," *Proceedings - IEEE International Conference on Robotics and Automation*, vol. 2, pp. 1321;1321 – 1326 vol.2;1326 vol.2, 06 1998.

[17] G. Nelson, A. Saunders, N. Neville, B. Swilling, J. Bondaryk, D. Billings, C. Lee, R. Playter, and M. Raibert, "Petman: A humanoid robot for testing chemical protective clothing," *Journal of the Robotics Society of Japan*, vol. 30, pp. 372–377, 01 2012.

[18] S. Kim, M. Kim, J. Lee, S. Hwang, J. Chae, B. Park, H. Cho, J. Sim, J. Jung, H. Lee, S. Shin, M. Kim, W. Choi, Y. Lee, S. Park, J. Oh, Y. Lee, S. Lee, M. Lee, and J. Park, "Team snu's control strategies for enhancing a robot's capability: Lessons from the 2015 darpa robotics challenge finals: Team snu's control strategies to enhancing robot's capability," *Journal of Field Robotics*, 12 2016.

[19] J. Englsberger, A. Werner, C. Ott, B. Henze, M. A. Roa, G. Garofalo, R. Burger, A. Beyer, O. Eiberger, K. Schmid, *et al.*, "Overview of the torque-controlled humanoid robot toro," in *Humanoid Robots (Humanoids), 2014 14th IEEE-RAS International Conference on*. IEEE, 2014, pp. 916–923.

[20] F. Negrello, M. Garabini, M. G. Catalano, J. Malzahn, D. G. Caldwell, A. Bicchi, and N. G. Tsagarakis, "A modular compliant actuator for emerging high performance and fall-resilient humanoids," in *15th IEEE RAS Humanoids Conference (HUMANOIDS2015)*, IEEE. IEEE, 2016, ¡p¿This work is supported by the WALK-MAN FP7-ICT-2013-10 European Commission project.¡/p¿. [Online]. Available: http://ieeexplore.ieee.org/stamp/stamp.jsp?arnumber=7363567

[21] J. Lim, H. Bae, J. Oh, I. Lee, I. Shim, H. Jung, H. Min Joe, O. Sim, T. Jung, S. Shin, K. Joo, M. Kim, K. Lee, Y. Bok, D.-G. Choi, B. Cho, S. Kim, J. Heo, I. Kim, and J.-H. Oh, "Robot system of drc-hubo+ and control strategy of team kaist in darpa robotics challenge finals," *Springer Tracts in Advanced Robotics*, pp. 27–69, 04 2018.

[22] K. Kaneko, M. Morisawa, S. Kajita, S. Nakaoka, T. Sakaguchi, R. Cisneros, and F. Kanehiro, "Humanoid robot hrp-2kai—improvement of hrp-2 towards disaster response tasks," in *Humanoid Robots (Humanoids), 2015 IEEE-RAS 15th International Conference on*. IEEE, 2015, pp. 132–139.

[23] C. Knabe, R. Griffin, J. Burton, G. Cantor-Cooke, L. Dantanarayana, G. Day, O. Ebeling-Koning, E. Hahn, M. Hopkins, J. Neal, J. Newton, C. Nogales, V. Orekhov, J. Peterson,

M. Rouleau, J. Seminatore, Y. Sung, J. Webb, N. Wittenstein, J. Ziglar, A. Leonessa, B. Lattimer, and T. Furukawa, "Team VALOR's ESCHER: A Novel Electromechanical Biped for the DARPA Robotics Challenge," *Journal of Field Robotics*, vol. 34, no. 5, pp. 912–939, 2017.

[24] M. Guihard and P. Gorce, "Biorobotic foot model applied to bipman robot," in *2004 IEEE International Conference on Systems, Man and Cybernetics (IEEE Cat. No.04CH37583)*, vol. 7, Oct 2004, pp. 6491–6496 vol.7.

[25] I.-W. Park, J.-Y. Kim, J. Lee, and J.-H. Oh, "Mechanical design of humanoid robot platform khr-3 (kaist humanoid robot 3: Hubo)," pp. 321 – 326, 02 2005.

[26] N. Tsagarakis, G. Metta, G. Sandini, D. Vernon, R. Beira, F. Becchi, L. Righetti, J. Santos-Victor, A. Ijspeert, M. Carrozza, and D. Caldwell, "icub - the design and realization of an open humanoid platform for cognitive and neuroscience research," *Journal of Advanced Robotics, Special Issue on Robotic platforms for Research in Neuroscience*, pp. 1151–1175, 2007.

[27] S. Lohmeier, T. Buschmann, and H. Ulbrich, "System design and control of anthropomorphic walking robot lt;emphasis emphasistype="italic" gt;lola lt;/emphasis gt;," *IEEE/ASME Transactions on Mechatronics*, vol. 14, no. 6, pp. 658–666, Dec 2009.

[28] J. Li, Q. Huang, W. Zhang, Z. Yu, and K. Li, "Flexible foot design for a humanoid robot," in *2008 IEEE International Conference on Automation and Logistics*, 2008, pp. 1414–1419.

[29] Y. Ogura, K. Shimomura, H. Kondo, A. Morishima, T. Okubo, S. Momoki, H. Lim, and A. Takanishi, "Human-like walking with knee stretched, heel-contact and toe-off motion by a humanoid robot," in *2006 IEEE/RSJ International Conference on Intelligent Robots and Systems*, Oct 2006, pp. 3976–3981.

[30] M. Y. Chuah and S. Kim, "Enabling force sensing during ground locomotion: A bio-inspired, multi-axis, composite force sensor using discrete pressure mapping," *IEEE Sensors Journal*, vol. 14, no. 5, pp. 1693–1703, 2014.

[31] M. Y. Chuah, M. Estrada, and S. Kim, "Composite force sensing foot utilizing volumetric displacement of a hyperelastic polymer," in *2012 IEEE/RSJ International Conference on Intelligent Robots and Systems*, Oct 2012, pp. 1963–1969.

[32] I. Ha, Y. Tamura, H. Asama, J. Han, and D. W. Hong, "Development of open humanoid platform darwin-op," in *SICE Annual Conference (SICE), 2011 Proceedings of*. IEEE, 2011, pp. 2178–2181.

[33] D. Gouaillier, V. Hugel, P. Blazevic, C. Kilner, J. Monceaux, P. Lafourcade, B. Marnier, J. Serre, and B. Maisonnier, "Mechatronic design of nao humanoid," in *Robotics and Automation, 2009. ICRA'09. IEEE International Conference on*. IEEE, 2009, pp. 769–774.

[34] K. Nishiwaki, T. Sugihara, S. Kagami, F. Kanehiro, M. Inaba, and H. Inoue, "Design and development of research platform for perception-action integration in humanoid robot: H6," in *Proceedings. 2000 IEEE/RSJ International Conference on Intelligent Robots and Systems (IROS 2000) (Cat. No.00CH37113)*, vol. 3, Oct 2000, pp. 1559–1564 vol.3.

[35] K. Nishiwaki, J. Kuffner, S. Kagami, M. Inaba, and H. Inoue, "The experimental humanoid robot h7: a research platform for autonomous behaviour," *Philosophical transactions. Series A, Mathematical, physical, and engineering sciences*, vol. 365, pp. 79–107, 02 2007.

[36] Y. Kim, B. Lee, J. Ryu, and J. Kim, "Landing force control for humanoid robot by time-domain passivity approach," *IEEE Transactions on Robotics*, vol. 23, no. 6, pp. 1294–1301, Dec 2007.

[37] C. Chevallereau, G. Abba, Y. Aoustin, F. Plestan, E. R. Westervelt, C. Canudas-De-Wit, and J. W. Grizzle, "Rabbit: a testbed for advanced control theory," *IEEE Control Systems Magazine*, vol. 23, no. 5, pp. 57–79, Oct 2003.

[38] S. Talebi, I. Poulakakis, E. Papadopoulos, and M. Buehler, "Quadruped robot running with a bounding gait," in *Experimental Robotics VII*, D. Rus and S. Singh, Eds. Berlin, Heidelberg: Springer Berlin Heidelberg, 2001, pp. 281–289.

[39] K. Kaneko, F. Kanehiro, S. Kajita, M. Morisawa, K. Fujiwara, K. Harada, and H. Hirukawa, "Slip observer for walking on a low friction floor," in *2005 IEEE/RSJ International Conference on Intelligent Robots and Systems*, Aug 2005, pp. 634–640.

[40] Y. Park, B. Chen, D. Young, L. Stirling, R. J. Wood, E. Goldfield, and R. Nagpal, "Bio-inspired active soft orthotic device for ankle foot pathologies," in *2011 IEEE/RSJ International Conference on Intelligent Robots and Systems*, Sept 2011, pp. 4488–4495.

[41] Y.-L. Park, C. Majidi, R. K. Kramer, P. Bérard, and R. J. Wood, "Hyperelastic pressure sensing with a liquid-embedded elastomer," 2010.

[42] Y. Park, B. Chen, and R. J. Wood, "Soft artificial skin with multi-modal sensing capability using embedded liquid conductors," in *SENSORS, 2011 IEEE*, Oct 2011, pp. 81–84.

[43] Y. Park, S. C. Ryu, R. J. Black, K. K. Chau, B. Moslehi, and M. R. Cutkosky, "Exoskeletal force-sensing end-effectors with embedded optical fiber-bragg-grating sensors," *IEEE Transactions on Robotics*, vol. 25, no. 6, pp. 1319–1331, Dec 2009.

[44] D. Kuehn, F. Grimminger, F. Beinersdorf, F. Bernhard, A. Burchardt, M. Schilling, M. Simnofske, T. Stark, M. Zenzes, and F. Kirchner, "Additional dofs and sensors for bio-inspired locomotion: Towards active spine, ankle joints, and feet for a quadruped robot," in *2011 IEEE International Conference on Robotics and Biomimetics*, Dec 2011, pp. 2780–2786.

[45] T. Mei, W. Li, Y. Ge, Y. Chen, L. Ni, and M. Ho Chan, "Integrated mems three-dimensional tactile sensor with large force range," *Sensors and Actuators A: Physical*, vol. 80, pp. 155–162, 03 2000.

[46] R. S. Dahiya, G. Metta, M. Valle, and G. Sandini, "Tactile sensing—from humans to humanoids," *IEEE Transactions on Robotics*, vol. 26, no. 1, pp. 1–20, Feb 2010.

[47] Z. Kappasov, J. A. Corrales, and V. Perdereau, "Tactile sensing in dexterous robot hands - review," *Robotics and Autonomous Systems*, vol. 74, pp. 195–220, 2015.

[48] M. Y. Chuah and S. Kim, "Improved normal and shear tactile force sensor performance via least squares artificial neural network (lsann)," in *2016 IEEE International Conference on Robotics and Automation (ICRA)*, May 2016, pp. 116–122.

[49] J. W. Guggenheim, L. P. Jentoft, Y. Tenzer, and R. D. Howe, "Robust and inexpensive six-axis force–torque sensors using mems barometers," *IEEE/ASME Transactions on Mechatronics*, vol. 22, no. 2, pp. 838–844, 2017.

[50] R. Tajima, D. Honda, and K. Suga, "Fast running experiments involving a humanoid robot," in *Robotics and Automation, 2009. ICRA'09. IEEE International Conference on*. IEEE, 2009, pp. 1571–1576.

[51] P.-B. Wieber, "Holonomy and nonholonomy in the dynamics of articulated motion," in *Fast motions in biomechanics and robotics*. Springer, 2006, pp. 411–425.

[52] C. P. Ridgewell, R. J. Griffin, T. Furukawa, and B. Lattimer, "Online estimation of friction constraints for multi-contact whole body control," in *2017 IEEE-RAS 17th International Conference on Humanoid Robotics (Humanoids)*, Nov 2017, pp. 347–352.

[53] S.-h. Lee and A. Goswami, "Momentum-based balance controller for humanoid robots on non-level and non-stationary ground," June 14 2016, uS Patent 9,367,795.

[54] P.-B. Wieber, R. Tedrake, and S. Kuindersma, *Modeling and Control of Legged Systems*. Springer, 2016.

[55] S. Kajita, M. Morisawa, K. Miura, S. Nakaoka, K. Harada, K. Kaneko, F. Kanehiro, and K. Yokoi, "Biped walking stabilization based on linear inverted pendulum tracking," in *Intelligent Robots and Systems (IROS), 2010 IEEE/RSJ International Conference on*. IEEE, 2010, pp. 4489–4496.

[56] P. Sardain and G. Bessonnet, "Forces acting on a biped robot. center of pressure-zero moment point," *IEEE Transactions on Systems, Man, and Cybernetics-Part A: Systems and Humans*, vol. 34, no. 5, pp. 630–637, 2004.

[57] M. A. Hopkins, D. W. Hong, and A. Leonessa, "Humanoid locomotion on uneven terrain using the time-varying divergent component of motion," in *2014 IEEE-RAS International Conference on Humanoid Robots*, Nov 2014, pp. 266–272.

[58] A. Werner, B. Henze, D. A. Rodriguez, J. Gabaret, O. Porges, and M. A. Roa, "Multi-contact planning and control for a torque-controlled humanoid robot," *IEEE International Conference on Intelligent Robots and Systems*, vol. 2016-Novem, pp. 5708–5715, 2016.

[59] L. Sentis, J. Park, and O. Khatib, "Compliant control of multicontact and center-of-mass behaviors in humanoid robots," *IEEE Transactions on Robotics*, vol. 26, no. 3, pp. 483–501, 2010.

[60] M. N. Orlin and T. G. McPoil, "Plantar pressure assessment," *Physical Therapy*, vol. 80, no. 4, pp. 399–409, 2000. [Online]. Available: http://dx.doi.org/10.1093/ptj/80.4.399

[61] P. R. Cavanagh and M. M. Rodgers, *Pressure Distribution Underneath the Human Foot*. Dordrecht: Springer Netherlands, 1985, pp. 85–95.

[62] R. Jones, "The human foot. an experimental study of its mechanics, and the role of its muscles and ligaments in support of the arch." vol. 68, no. 4, pp. 1–39, 1941.

[63] G. De Magistris, S. Miossec, A. Escande, and A. Kheddar, "Design of optimized soft soles for humanoid robots," *Robotics and Autonomous Systems*, vol. 95, pp. 129–142, 2017.

[64] Y. Tenzer, L. P. Jentoft, and R. D. Howe, "Inexpensive and easily customized tactile array sensors using mems barometers chips," *IEEE Robot. Autom. Mag*, vol. 21, no. 3, pp. 89–95, 2014.

[65] R. R. Ma, J. T. Belter, and A. M. Dollar, "Hybrid deposition manufacturing: design strategies for multimaterial mechanisms via three-dimensional printing and material deposition," *Journal of Mechanisms and Robotics*, vol. 7, no. 2, p. 021002, 2015.

[66] A. Ananthanarayanan, S. Foong, and S. Kim, "A compact two dof magneto-elastomeric force sensor for a running quadruped," in *2012 IEEE International Conference on Robotics and Automation*, May 2012, pp. 1398–1403.

[67] D. C. Liu and J. Nocedal, "On the limited memory bfgs method for large scale optimization," *Mathematical Programming*, vol. 45, no. 1, pp. 503–528, Aug 1989. [Online]. Available: https://doi.org/10.1007/BF01589116

[68] T.-F. Lu, G. C. Lin, and J. R. He, "Neural-network-based 3d force/torque sensor calibration for robot applications," *Engineering Applications of Artificial Intelligence*, vol. 10, no. 1, pp. 87 – 97, 1997. [Online]. Available: http://www.sciencedirect.com/science/article/pii/S0952197696000693

[69] D. Marquardt, "An algorithm for least-squares estimation of nonlinear parameters," *Journal of the Society for Industrial and Applied Mathematics*, vol. 11, no. 2, pp. 431–441, 1963. [Online]. Available: https://doi.org/10.1137/0111030

[70] F. Pedregosa, G. Varoquaux, A. Gramfort, V. Michel, B. Thirion, O. Grisel, M. Blondel, P. Prettenhofer, R. Weiss, V. Dubourg, J. Vanderplas, A. Passos, D. Cournapeau, M. Brucher, M. Perrot, and E. Duchesnay, "Scikit-learn: Machine learning in Python," *Journal of Machine Learning Research*, vol. 12, pp. 2825–2830, 2011.

[71] C. DUDESCU and L. Racz, "Effects of raster orientation, infill rate and infill pattern on the mechanical properties of 3d printed materials," *ACTA Universitatis Cibiniensis*, vol. 69, 12 2017.

[72] M. R. Berenbaum, D. Sadava, H. C. Heller, and D. M. Hillis, *Life. the science of biology*. Sinauer Associated, Inc., 2011.